Variability of aerosol optical properties derived from in situ aircraft measurements during ACE-Asia

Theodore L. Anderson[1]

Joint Institute for the Study of the Atmosphere and Oceans, University of Washington, Seattle, Washington, USA

Sarah J. Masonis, David S. Covert, and Norman C. Ahlquist

Department of Atmospheric Sciences, University of Washington, Seattle, Washington, USA

Steven G. Howell, Antony D. Clarke, and Cameron S. McNaughton

Department of Oceanography, University of Hawaii, Honolulu, Hawaii, USA

[1] Airborne measurements of aerosol light scattering (using nephelometers) and absorption (using particle/soot absorption photometers; PSAPs) in the Asian outflow region are presented. Aerosol particles were sampled through a new low turbulence inlet that proved very effective at transmitting coarse-mode particles. Noise and artifacts are characterized using in-flight measurements of particle-free air and measurements with identical instruments operated in parallel. For example, the sensitivities of PSAP noise to changing altitude, changing relative humidity (RH), and particle-loading on the internal filter are quantified. On the basis of these and previous instrument characterizations, we report averages, variations, and uncertainties of optical properties, focusing on data from approximately 300 level-leg samples obtained during 19 research flights in the spring of 2001. Several broad patterns emerge from this analysis. Two dominant components, fine-mode pollution and coarse-mode mineral dust, were observed to vary independently when separated using a cut point of 1 μm aerodynamic diameter at low RH. Fine-mode pollution was found to be moderately absorbing (single scatter albedo at low RH and 550 nm, $\omega = 0.88 \pm 0.03$; mean and 95% confidence uncertainty) and moderately hygroscopic (relative increase in scattering from 40% to 85% RH, $f_{RH} = 1.7 \pm 0.2$), while coarse-mode dust was found to have very low absorption ($\omega = 0.96 \pm 0.01$) and to be almost nonhygroscopic ($f_{RH} = 1.1 \pm 0.1$). These and other optical properties are intended to serve as constraints on optical models of the Asian aerosol for the purpose of satellite retrievals and calculations of direct radiative effects. *INDEX TERMS:* 0305 Atmospheric Composition and Structure: Aerosols and particles (0345, 4801); 0360 Atmospheric Composition and Structure: Transmission and scattering of radiation; 0365 Atmospheric Composition and Structure: Troposphere—composition and chemistry; 0394 Atmospheric Composition and Structure: Instruments and techniques; 1610 Global Change: Atmosphere (0315, 0325); *KEYWORDS:* aerosol, optical, variability, in situ, ACE-Asia, dust

1. Introduction

1.1. Approach

[2] We present airborne measurements of the scattering and absorption properties of aerosol in the Asian outflow region of the western Pacific. These were measured from the National Center for Atmospheric Research C-130 aircraft during the Aerosol Characterization Experiment (ACE)-Asia in the spring of 2001 (28 March to 6 May). This introductory section outlines the goals of our study and defines the properties to be discussed. Section 2 reports on the nature and quality of the measurements and provides details of the data reduction procedures. Section 3 presents a statistical overview of the measured optical properties, including uncertainty, variability, and correlation analysis. In addition, it provides a preliminary characterization of the two dominant aerosol types encountered: pollution and mineral dust. Section 4 summarizes the results and suggests directions for future research.

[3] Aerosol radiative properties consist of the wavelength-dependent scattering coefficient, $\sigma_{sp}(\lambda)$, the wavelength-dependent absorption coefficient, $\sigma_{ap}(\lambda)$, each with

---

[1]Now at Department of Atmospheric Sciences, University of Washington, Seattle, Washington, USA.

units of inverse distance (Mm^{-1} herein), and the dimensionless scattering phase function, $P(\phi)$. These properties are known to depend strongly on particle size distribution, chemical composition, and on the ambient relative humidity (RH). Our overall goal is to characterize these properties over the solar spectrum and to separate the effects of natural and anthropogenic aerosols in order to understand the direct, shortwave impact of anthropogenic aerosols on regional and global energy balance. Toward this goal, we discuss herein measurements of aerosol scattering and absorption properties at specific wavelengths, specific RH's, over specific angular ranges, and over specific portions of the aerosol size distribution. Solving the radiative transfer problem requires a complete aerosol optical model. The measurements discussed herein provide key constraints on such a model. Their value stems from (1) the fact that the measured properties apply to the aerosol population, thereby integrating over complexities of size, shape, chemistry, and state of mixture, (2) the robust nature of the measurements, especially the ability to provide continuous data with well-defined noise and overall uncertainty, and (3) high time resolution to allow assessment of spatiotemporal variability and correlations among parameters.

[4] Scattering properties are measured using various types of nephelometers, and light absorption is measured with the Particle Soot Absorption Photometer (PSAP, Radiance Research, Seattle, WA). These instruments and the basic measurement strategy adopted herein have been described in previous papers [*Anderson et al.*, 1999, 2000; *Masonis et al.*, 2002, 2003]. Key aspects include (1) separate analysis of the submicron aerosol using a cut point of 1 μm aerodynamic diameter at low RH, (2) most measurements performed at low relative humidity (RH < 40%) in order to reduce the effects of RH changes as a source of variation, (3) RH-induced variation studied separately using deliberate humidification, and (4) frequent measurement of particle-free air in order to assess instrumental noise and calibration stability.

[5] Confidence that these measurements are well understood is based, in part, on ground-based studies of instrumental noise and calibration stability for the TSI, Inc (St Paul, MN) model 3563 nephelometer [e.g., *Anderson and Ogren*, 1998] and the PSAP [e.g., *Anderson et al.*, 1999]. An important aspect of the present study is to extend this work to the airborne setting and to the Radiance Research (Seattle, WA) model M903 nephelometer. The latter device measures at only one wavelength and, as we will show, displays lower sensitivity and less calibration stability than the TSI nephelometer as well as a significant discrepancy when measuring supermicron particles. On the other hand, it provides a comparable measurement of submicron light scattering and is well-suited to measurements at multiple, controlled humidities owing to its lower flow rate and negligible heating of the sample stream. PSAP performance is explored using measurements of filtered air and measurements with two instruments operating in parallel. These data allow us to quantify previous observations that PSAP noise is sensitive to altitude and RH changes and to particle loading on the filter. In addition, we provide further performance information on the 180-nephelometer.

1.2. Instruments and Measured Quantities

[6] Total scattering, σ_{sp}, and hemispheric (i.e., $90°-180°$) backscattering, σ_{bsp}, at three wavelengths (450, 550, and 700 nm) were measured with a pair of TSI model 3563 nephelometers. The first, denoted N_{tot}, measures all sampled particles while the second, denoted N_{sub}, measured only the submicron portion of the aerosol. Total scattering at high and low RH was measured with a pair of Radiance Research model M903 nephelometers. These units were modified by replacing the optical filter at the light detector with a Corion CA-550 80 nm bandpass filter. The effective wavelength, accounting for the combined sensitivities of flash lamp, Corion filter, and photomultiplier tube, was measured using a spectrophotometer and determined to be 540 ± 3 nm. The first unit, denoted N_{dry}, measured at low RH (nearly always less than 40%) while the second, denoted N_{wet}, measured at $85 \pm 2\%$ RH. The backscattering intensity at 180°, β_p, was measured at 532 nm with a custom nephelometer [*Doherty et al.*, 1999], denoted N_{180}. Light absorption, σ_{ap}, at 550 nm was measured with a pair of PSAPs, the first measuring the total aerosol and denoted A_{tot} while the second measured only the submicron aerosol and is denoted A_{sub}. The effective wavelength of the PSAP was measured using a spectrophotometer and determined to be 570 ± 2 nm. However, the unit is calibrated with respect to σ_{ap} at 550 nm [*Bond et al.*, 1999] and that is what is reported in this paper. (Potential error associated with this wavelength discrepancy is included in the uncertainty analysis.)

[7] The parameters above represent extensive aerosol properties, that is, properties that vary in proportion to aerosol concentration. The key intensive properties to be discussed herein are derived from these extensive properties. They are, the submicron fraction of scattering at 550 nm and low RH,

$$FF_{scat} = \frac{\sigma_{sp}(D_{aero} < 1\mu m)}{\sigma_{sp}(total)} \qquad (1)$$

the scattering Ångström exponent from 550 to 700 nm at low RH,

$$\mathring{a} = -\frac{\log\{\sigma_{sp}(550)/\sigma_{sp}(700)\}}{\log\{550/700\}}. \qquad (2)$$

the hemispheric (i.e., $90°-180°$) backscatter fraction at 700 nm and low RH,

$$b = \frac{\sigma_{bsp}}{\sigma_{sp}} \qquad (3)$$

the single scattering albedo at 550 nm and low RH,

$$\omega = \frac{\sigma_{sp} + \sigma_{ap}}{\sigma_{sp}} \qquad (4)$$

the scattering humidification factor at 540 nm,

$$f_{RH} = \frac{\sigma_{sp}(RH = 85\ \%)}{\sigma_{sp}(RH = 40\ \%)} \qquad (5)$$

and the extinction-to-backcatter ratio (or lidar ratio) at 532 nm and low RH,

$$S = \frac{\sigma_{sp} + \sigma_{ap}}{\beta_p} \qquad (6)$$

[8] Small adjustments for wavelength and/or RH are required to calculate f_{RH} (because the measurements are not always made at exactly 40% and 85% RH) and S (because σ_{sp} and σ_{ap} are measured at 550 nm and the N_{180} instrument is often at slightly higher RH than N_{tot}.) All wavelength conversions are made assuming an exponential dependence, as in equation (2). RH adjustments are accomplished by assuming that the hydration effect on scattering follows an exponential form,

$$\frac{\sigma_{sp}\left(RH_{high}\right)}{\sigma_{sp}\left(RH_{low}\right)} = \left[\frac{1\text{-}RH_{low}}{1\text{-}RH_{high}}\right]^{\gamma} \tag{7}$$

The scattering measurements by the nephelometers N_{wet} and N_{dry} were used to determine the exponent, γ, and this, in turn, was used to adjust the measured scattering values to 85% and 40%, respectively, in order to calculate f_{RH}. The γ parameter can be considered an alternate form of the measured humidification parameter. However, f_{RH} more closely reflects the actual, two-point measurement performed herein.

2. Methods

2.1. Flight Patterns

[9] The ACE-Asia campaign was intended to characterize the aerosols flowing from the Asian continent over the Pacific, especially with regard to those optical and chemical properties that control direct, shortwave, radiative forcing. Within this broad mandate, a large number of specific experimental objectives competed for priority on individual flights by the C-130 aircraft. These included in situ characterization of the major aerosol types (dust, industrial pollution, biomass burning), measurements of radiative flux perturbations induced by the aerosol, testing transport models either by flying upwind and downwind of specific source regions (e.g., Korea and Japan) or by flying across predicted gradients in concentration, and conducting coordinated measurements with other platforms (satellite, aircraft, ship, or land-based). Some of these objectives are mutually exclusive. For example, chemical characterization requires level legs within aerosol layers and is indifferent to clouds aloft, whereas radiation measurements require vertical profiles and the absence of clouds aloft. Similarly, the clear-sky region within a satellite field-of-view may not coincide with where the transport models predict an interesting gradient of aerosol concentration. As a result, individual flights pursued different specific objectives and the overall data set from the 19 flights cannot be said to represent a systematic or representative sampling of the aerosol in the region. (This is consistent with the exploratory nature of the campaign.) Moreover, there is likely to be a positive bias in aerosol concentration because C-130 deliberately sought out sampled regions where significant aerosol phenomena were anticipated.

[10] Despite these caveats, data from the 19 flights do represent a large and diverse set of measurements from this region. The geographical diversity is shown in Figure 1, which displays the location of each major level leg (lines) and each significant vertical profile (circles).

2.2. Measurement Design and Details

2.2.1. Inlet and Plumbing Configuration

[11] Figure 2 provides a simplified schematic of the plumbing and instrument arrangement. Aerosol particles were brought into the airplane via a newly developed low turbulent inlet (LTI) [Lafleur, 1998]. This inlet as well as the plumbing arrangement was optimized for the efficient sampling of coarse-mode particles. All sample tubing was conductive material, either metal or carbon-impregnated silicone. Sharp bends and abrupt diameter changes were avoided. Size-dependent plumbing losses were assessed after the experiment using monodispersed oil droplets. Results of these tests are given in section 2.2.4. In general, particle transmission efficiencies were excellent up to about 2 μm aerodynamic diameter, from 2 to 10 μm, LTI enhancement and plumbing losses largely canceled each other, while, above 10 μm, plumbing losses led to rapidly declining transmission efficiencies. The only component that seems to have been poorly designed for efficient transmission of large particles was a short section of bellows-style, flexible metal tubing located just downstream of the LTI. This component has a ribbed inner surface which caused significant large-particle deposition in the oil droplet tests.

[12] From the LTI, sample air passed through a zeroing system consisting of a manual ball valve that, when closed, diverted the entire sample flow through a HEPA filter, thereby removing the particles. Data from a zero test during RF01 (Research Flight 1) are shown in Figure 3. Frequent, in-flight zero tests serve three functions. (1) They test plumbing integrity. A positive signal on any instrument would indicate cabin air leaking into the plumbing. Following a few seconds flushing time, particle counts were always less than 1 per cc during these tests. Figure 2 also shows a needle (constriction) valve downstream of the zero filter; this was used to perform leak tests on the ground while maintaining the sample plumbing at low pressure. (2) In-flight zero tests provide data for assessing instrumental noise and, for the nephelometers, calibration errors. This will be discussed further in section 2.2.2. (3) Finally, because these tests represent a step change in aerosol concentration, they allow instrument response times to be studied and allow accurate time-synchronization of all instruments. Using these data the time-stamp associated with each measurement was adjusted so that it corresponds to the time when the aerosol sample was entering the aircraft inlet. These adjustments ranged from 12 to 30 s and take into account both the lag time associated with delivering the sample through the plumbing and instrument response time due to either its internal volume or built-in data smoothing. Response times are discussed further in section 2.2.3.

[13] Downstream of the zeroing system, the flow was split three ways. The milled, aluminum flow-splitter was custom-designed to divide the flow isokinetically and, subsequently, to expand or contract the flow at less than a 7° half-angle to accommodate the next section of sample tubing. Several other flow splitters, not shown in Figure 2, were incorporated into the plumbing arrangement; all followed these same design principles, which derive from the work of Gupta and McFarland [2001].

[14] Sample flow then went to three different measurement systems shown in Figure 2. The systems labeled "Total" and "Sub" used identical instrumentation, a TSI 3563 nephelometer and a PSAP, to measure the low RH scattering and absorption properties of the total aerosol and the submicron aerosol. As stated earlier, the term
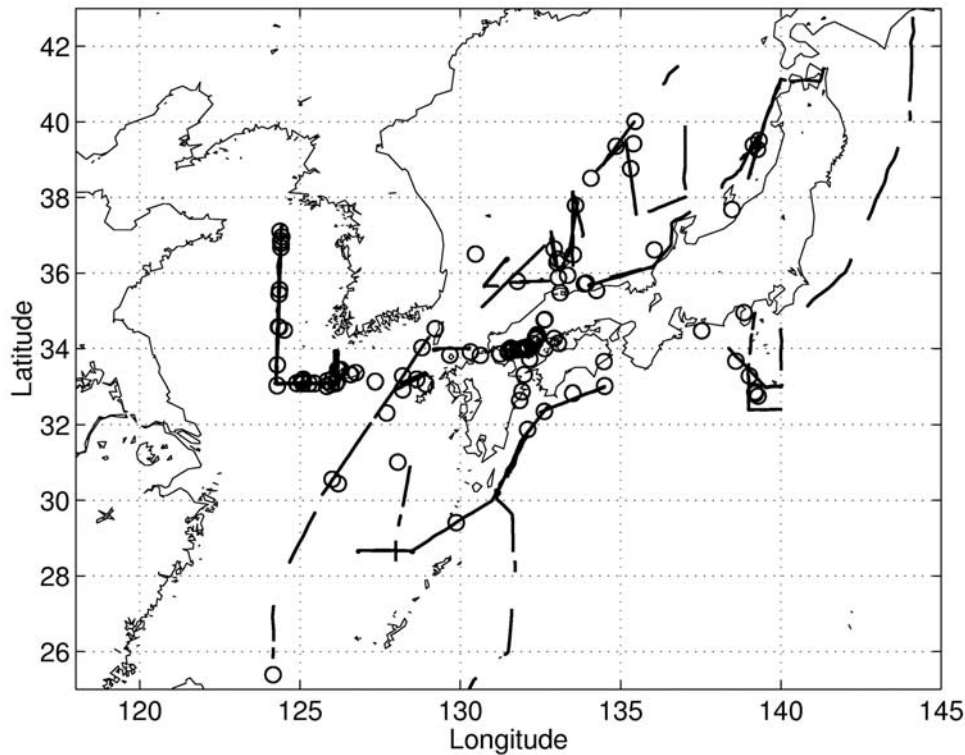
Figure 1. Location of all significant level-legs (line segments) and profiles (circles) flown by the C-130 during the ACE-Asia campaign. The plane was based in Iwakuni, Japan.

"submicron" refers, throughout this paper, to the portion of the aerosol smaller than 1.0 μm aerodynamic diameter at low RH. To select this portion of the aerosol, supermicron particles were removed with a multiorifice impactor following the design of *Berner et al.* [1979]. A greased substrate was used to prevent particle bounce. The ball valve shown in Figure 2 was normally closed (forcing the sample flow through the impactor) but was opened periodically so that the "Sub" and "Total" systems were operating in parallel. The data thus obtained on measurement precision are critical to evaluating the uncertainty of the measurement of supermicron scattering and absorption, which is obtained by differencing the "Total" and "Sub" measurements. As shown in Figure 2, the "Total" sample stream passed initially through the custom, 180-nephelometer [*Doherty et al.*, 1999]. This nephelometer uses laser illumination and thus does not heat the flow. In addition, potential particle losses during transit through the 180-nephelometer were minimized by various modifications to the nephelometer inlet, outlet, and plumbing. Data obtained during parallel operation (see section 2.4.1) showed no detectable loss of large particles.

[15] All measurements discussed so far were made at low RH in order to provide a standard reference condition and to eliminate RH as a source of variation. Low RH was achieved passively by allowing the sample to warm from ambient toward cabin temperature. In almost all cases, the RH inside the nephelometers was 40% or below. On one flight (RF16) the boundary layer was particularly warm and humid and this led to much higher measurement RH. The highest sample-stream RH occurs in the 180-nephelometer because it is upstream of other instruments and it does not

heat. For the purpose of this paper, we eliminate data whenever RH inside the 180-nephelometer exceeds 60%.

[16] In order to measure the effect of humidity on mid-visible light scattering, sample air was passed (in parallel) through a pair of single-wavelength, Radiance Research nephelometers. One, N_{dry}, operated at the same low RH as the rest of the system. The other, N_{wet}, operated downstream of a humidifier that maintained nephelometer RH at 85 ± 2%. This is the system denoted "fRH" on Figure 2. The humidifier is similar in design to that described by *Gassó et al.* [2000]. The airstream passes through a 1/4" ID Teflon tube that is permeable to water vapor and that is surrounded by liquid water. Variable heating of this liquid controls the flux of water vapor into the sample air stream. Humidity in both nephelometers is measured with a capacitive, thin-film polymer device (model Humitter 50Y, Vaisala, Inc, Woburn, MA). For N_{wet}, RH was measured at both the inlet and the outlet in order to assess RH gradients. The Radiance Research nephelometer has lower sensitivity than the TSI, however, it has two advantages in terms of measuring aerosol hydration. First, it uses flash-lamp illumination, which transmits much less energy to the sample stream and thereby causes little or no heating. (Indeed, measured temperature was slightly lower at the outlet of N_{wet} than at the inlet.) Second, it is a physically smaller instrument designed for a much lower flow rate. (We used 6 L min^{-1}, which can be compared to 30 L min^{-1} used for the TSI nephelometers.) A smaller flow is easier to humidify. The "fRH" system normally measured the total aerosol, however, as shown on Figure 2, a ball valve and 1 μm impactor were located upstream of this system to allow periodic measurement of the hygroscopicity of the submicron aero-
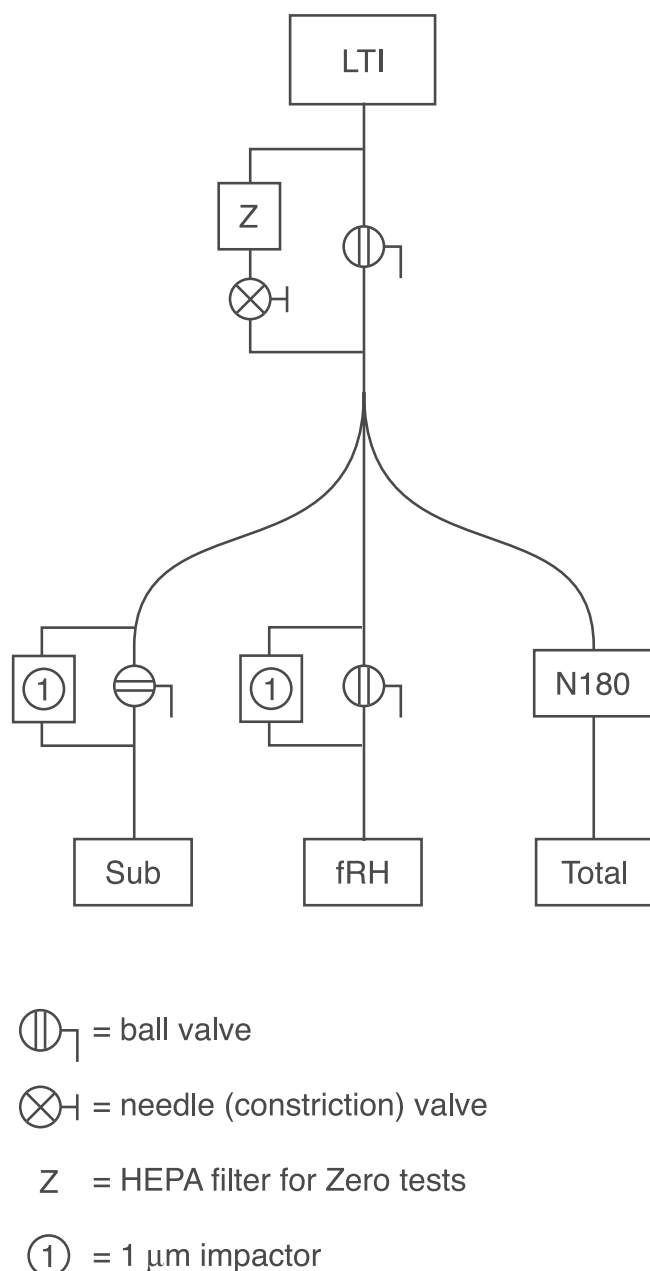
Figure 2. Aerosol sampling schematic. Components shown are LTI, low turbulence inlet; Z, HEPA filter used for zero tests with particle-free air; circled 1, the 1-μm impactors for removing supermicron particles; Sub, nephelometer and PSAP used to measure submicron aerosol; fRH, dual nephelometers and humidifier used to measure aerosol hygroscopicity; 180, 180° backscatter nephelometer; Total, nephelometer and PSAP used to measure the total aerosol. For flights 1–5, both PSAPs were connected to the "Total" system to obtain replicate measurements.

sol. By switching back and forth on many of the longer level-legs, the hygroscopic properties of the supermicron aerosol could be estimated as well.

2.2.2. Response Times

[17] Data were recorded every 2 s, but information on ambient variation depends on the response time of each
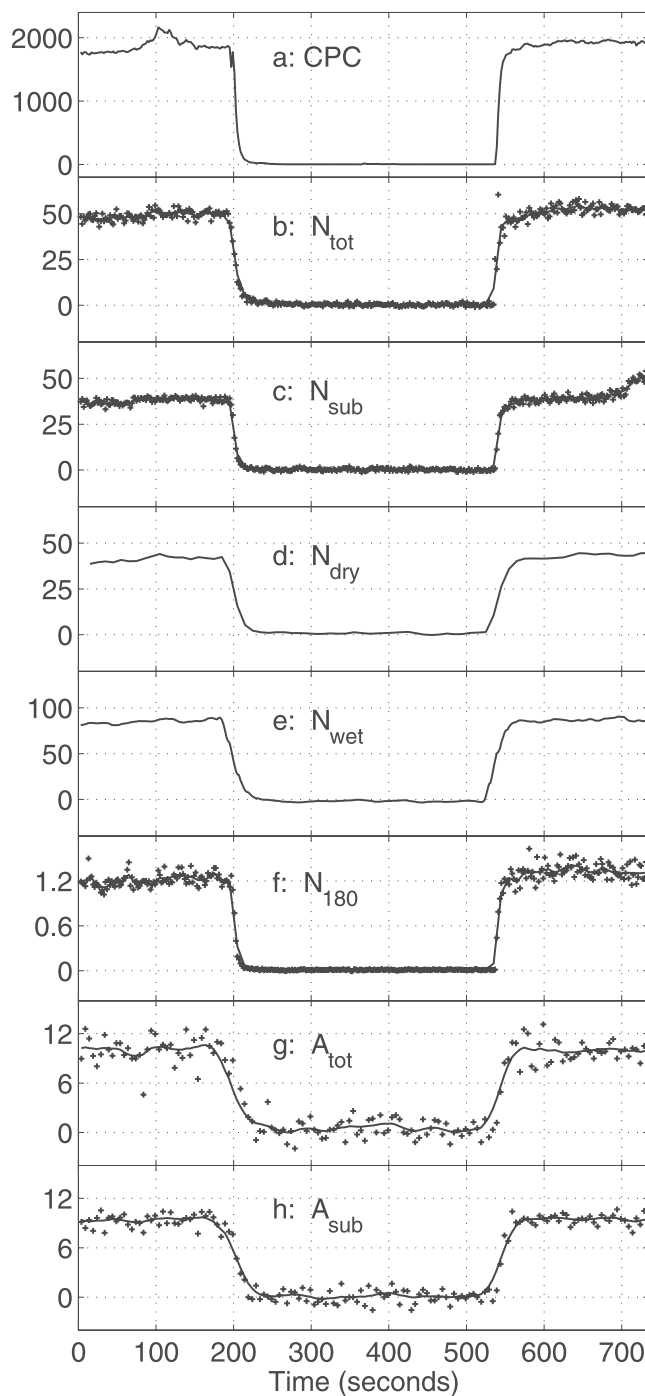

Figure 3. Example from flight 1 of an in-flight zero test. The ball valve immediately down stream of the LTI (Figure 2) was closed at time labeled 200 and reopened at time 430 (time in seconds, arbitrary starting point). While closed, sample air is forced through a filter, removing the particles. Time synchronization, response times, noise levels, and calibration errors can be assessed with these data, as discussed in text. Time resolution of data are (a) 2-s, (b, c, and f) points are 2-s, lines are 10-s, (d and e) 10-s data but with built-in 30-s smoothing, (g-h) points are 5-s, lines are 10-s data but with built-in 30-s smoothing.

instrument. This depends on physical flushing times for each instrument, on instrumental noise, and on the smoothing function employed in data reduction. Figure 3 shows data from a zero test, where the sudden turning of a ball valve represents a step change in aerosol concentration much sharper than would be expected to occur in the atmosphere (except, possibly, at the boundaries of clouds or fresh plumes.) The solid lines in Figure 3 show the processed data at 10-s resolution, except for panel a, where CPC data is shown at 2-s resolution. The dots on Figures 3b, 3c, and 3f–3h show that higher resolution data contain mostly noise. The flushing time of the TSI nephelometer, based on plug flow at 30 L min^{-1}, is roughly 6 s. (The equivalent flushing time for the Radiance Research nephelometer at 6 L min^{-1} is 5 s.) The CPC was located downstream of the 180-nephelometer ("N_{180}" on Figure 2) and data from this instrument indicate an e-folding response time of 9 s. Thus, in terms of instrument flushing times, successive 10-s data points can be taken as independent measurements of ambient aerosol concentration. Clearly, noise levels for the TSI nephelometers ("N_{tot}", "N_{sub}", and "N_{180}", Figures 3b, 3c, and 3f) are sufficiently low that variations at 10-s resolution are resolved. However, data from the Radiance Research nephelometers ("N_{dry}" and "N_{wet}", Figures 3d and 3e) as well as the PSAPs ("A_{tot}" and "A_{sub}", Figures 3g and 3h) were processed with 30-s smoothing in order to reduce instrumental noise. Thus successive 10-s data points for these instruments are not independent and the effective response time is 30 s in each case. Given the typical flight speed of 100 m s^{-1}, 10- and 30-s response times correspond to 1- and 3-km spatial resolution, respectively.

2.2.3. Size-Dependent Sampling Efficiencies

[18] An aircraft inlet must decelerate the sample flow prior to distributing it to the instruments. Traditional, solid diffuser inlets have poor transmission efficiencies for coarse mode particles [*Huebert et al.*, 1990; *Blomquist et al.*, 2001]. In ACE-Asia, coarse mode dust was expected (and found) to be a major contributor to aerosol mass and optical properties. In order to effectively sample these particles, a newly developed low turbulence inlet (LTI) [*Lafleur*, 1998] was used. The LTI maintains laminar flow during deceleration by sucking away a major fraction (~70%) of the incoming air through porous walls of the diffuser. This eliminates the major cause of large-particle losses; indeed, it creates the opposite problem, transmission efficiencies (which can be calculated accurately due to the laminar flow conditions) rise steeply above unity for particle sizes above a few microns aerodynamic diameter (Figure 4). Balancing this, however, is that fact that large particles are preferentially lost in sample tubing due to gravitational settling and impaction at bends. These losses were quantified by reassembling the sample plumbing in a laboratory and measuring the size-dependent transmission efficiency of oil droplets. Results (Figure 4) indicate that transmission efficiency to the optical instruments peaks at a value of 1.35 for a size of 5 microns aerodynamic diameter. However, coarse mode particles will naturally be distributed over a broad range of sizes. Using Mie calculations for lognormal size distributions, assuming volume-mean geometric diameters up to 10 μm, and assuming a geometric standard deviation of 2, we estimate that the size-dependent, net sampling efficiencies shown in Figure 4 cause coarse mode scattering
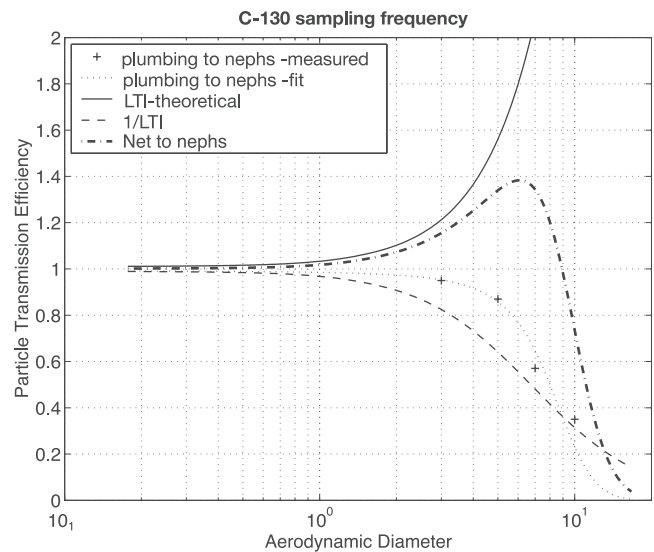

Figure 4. Inlet and plumbing transmission efficiency as a function of aerodynamic diameter. LTI data are based on theoretical calculations, which are considered accurate given the measured, laminar flow conditions. Plumbing data are based on laboratory measurements with oil drops using the same flow rates and plumbing components as in the field. The four measurement points have been fit with the equation E = 0.5 − 0.5*tanh(A(D − D_{50})), where E is transmission efficiency, A is set to 0.3, and D_{50} is set to 8 μm. Net transmission efficiency is the product of LTI and plumbing efficiencies. The dashed line shows the inverse of the LTI efficiency to emphasize where the two terms compensate.

to be enhanced by about 10% but do not cause significant changes in the intensive optical properties of the coarse mode. We do not correct for this (modest) effect because we consider the uncertainty of such a correction to be unknown and potentially larger than the correction itself. Two other papers in this issue provide independent evidence that the enhancement of coarse-mode scattering was modest (~10% or less). One compares a large number of nephelometer/PSAP-derived extinction profiles to profiles derived from an on-board Sun photometer [*Redemann et al.*, 2003]. The other compares the nephelometer/PSAP extinction and 180-backscatter profiles for one flight to profiles derived from ground-based lidar [*Murayama et al.*, 2003].

2.2.4. Leaks

[19] The question of plumbing leaks is important whenever instruments that sample the ambient air (commonly denoted "in situ" instruments) are operated inside a pressurized aircraft. Under these conditions, leaks allow cabin air to be introduced into the sample stream, which can either dilute or contaminate the sample, depending on the substance being monitored, its concentration in the cabin air, and its ability to penetrate the leak. (Note, for example, that coarse-mode particles are unlikely to be transmitted through leaks.) Even more important for this experiment, leaks in the PSAP instrument appear to make it much more subject to pressure-induced artifacts.

[20] Leak rates were determined by drawing a partial vacuum on the instruments (components and/or the entire

sampling system) and measuring the rate at which this partial vacuum goes away. The volume leak flow rate, dV/dt (L min^{-1}), is then calculated as,

$$\frac{dV}{dt} = \frac{dP}{dt} \frac{V}{P_{test}}$$ (8)

where dP/dt is the measured leak rate in terms of pressure increase per unit time (mb/min), V is the volume of the test plumbing (liters), and P_{test} is the pressure inside the test plumbing (mb). Obviously, the leak rate is a strong function of the pressure differential, ΔP (mb), between the ambient and test plumbing. For ACE-Asia, the C-130 operated almost exclusively between the surface and 500 mb such that ΔP was essentially always less than 450 mb. Thus we present leak rate results for a ΔP of 450 mb. Complete leak rate data were not obtained; however, measurements that were made (Table 1) are adequate to show that leaks for all instruments were 1% or less.

[21] Minimizing the PSAP leak rate is important for airplane deployment in order to minimize measurement artifacts associated with pressure changes. Two main steps were taken to achieve this: use of a modified filter holder and sealing the optical-fiber bundle with glue. The original filter holder uses an O-ring pressing down upon the glass-fiber filter material, which does not create an adequate seal when subjected to pressure differences of 100 mb or more. A modified holder, available from the manufacturer, uses a piston-type O-ring arrangement creating an air seal that is independent of the filter. Even with this modification, however, significant leaks were discovered and were traced to the epoxy-coated, optical-fiber bundle that is used to illuminate the filter. These micropore leaks were virtually eliminated by painting the optical-fiber bundle with ordinary rubber cement while drawing a vacuum on the inside. In addition, the O-rings of the mass flowmeter were regreased and the plumbing connections to the optical block were improved by replacing the stiff polyethylene tubing with flexible, conductive, black silicone tubing. In the end, an excellent seal was obtained on one unit (A_{sub}) and an adequate, though somewhat less ideal seal was obtained on the other (Table 1). A significant difference in noise levels between these two units was observed during the campaign (see below), which may be partially due to the difference in leak rate.

2.3. Data Reduction

[22] The general approach to calibration and correction for instrumental nonidealities has been described in previous publications [e.g., *Anderson et al.*, 1999, 2000; *Masonis et al.*, 2002, 2003]. Here we give a brief overview and highlight aspects unique to this campaign.

2.3.1. Calibration and Calibration Stability

[23] Nephelometer calibrations followed the procedures outlined by *Anderson and Ogren* [1998]. Calibration gases (air and CO_2) were measured eight times during the campaign, on nonflight days. From these measurements, offset and slope corrections were calculated and applied to the data from each flight. Filtered air measurements obtained on every flight provide diagnostic information on calibration stability. Calibration drift was found to be almost negligible for the TSI model 3563 nephelometers, N_{tot} and N_{sub}, but not for the Radiance Research model M903 nephelometers, N_{dry} and N_{wet}, nor for the custom,

Table 1. Leak Rates[a]

Test	V, L	P_{test}, mb	dP/dt, mb/min	dV/dt, L min^{-1}	Q_{sample}, L min^{-1}	Fractional Leak
Rack[b]	21	550	3.1	0.12	60	0.2%
A_{sub} (PSAP)[c]	1	510	0.92	0.002	1	0.2%
A_{tot} (PSAP)[d]	–	550	–	0.010	1	1.0%
N_{wet} (neph)	1.5	520	20.0	0.057	6	1.0%
N_{dry} (neph)	1.5	330	0.62	0.003	6	0.05%

[a]All tests performed at $\Delta P = 450$ mb or more to simulate worst case leak rates. Q_{sample} is the sample flow rate during normal operation (L min^{-1}). Fractional leak is $(dV/dt)/Q_{sample}$.

[b]Entire sampling system from the zeroing valve through all optical instruments except the dry and humidified nephelometers (N_{dry}, N_{wet}) and the humidifier. Volume is estimated as three TSI nephelometers at 7 L each.

[c]PSAP internal volume is trivial (less than 0.1 L) so a 1 L canister was attached to the test plumbing in order to achieve a precise leak-rate measurement.

[d]Leak rate for the A_{tot} unit was not measured directly but obtained by difference from rack measurements with and without the PSAPs included and by knowledge of the A_{sub} leak rate.

180-backscatter nephelometer, N_{180}. Because filtered air measurements were made at multiple pressures (i.e., multiple altitudes), we are able to derive secondary offset and slope correction factors in cases where significant calibration errors were discovered. Using this approach, secondary calibration adjustments were made for N_{dry} and N_{wet} on the first two flights and were made for N_{180} throughout the campaign.

[24] Calibration of the PSAP instrument requires both a nephelometer and an extinction cell to derive, by difference, a reference value of light absorption. At present, this is difficult to accomplish in the field. We relied on the laboratory calibration results of *Bond et al.* [1999] and the assumption that this calibration applies to all PSAP units. This assumption is partially tested by the duplicate absorption measurements obtained during the first five flights of this campaign (Table 2a and Figure 5b).

2.3.2. Corrections for Nephelometer Angular Nonidealities

[25] Scattering values measured by the TSI nephelometers were adjusted for angular nonidealities as follows. First, submicron scattering was adjusted based on the measured wavelength dependence of scattering, using the formulas in Table 4b of *Anderson and Ogren* [1998]. Next the supermicron scattering was calculated by subtracting unadjusted N_{sub} from N_{tot}. Supermicron scattering was then adjusted based on the formulas in Table 4a of *Anderson and Ogren* [1998]. Note that these corrections are large and quite uncertain, e.g., the correction for supermicron scattering at 550 nm is 1.51 with a 95% confidence uncertainty of ±0.28.

[26] For the Radiance Research (RR) nephelometers, no correction for angular nonidealities was made since these instruments were only used to provide a relative measure, that is, the ratio of high RH scattering to low RH scattering. See section 2.4.2 for further details.

[27] The measurement of β_p by N_{180} also involves a small angular nonideality in that the instrument actually responds to scattering integrated from ~176° to ~178°. The conversion of this flux quantity to the radiance quantity β_p is incorporated into the gas calibration, and for most aerosols $\sigma_{176°-178°}$ is an excellent proxy for β_p [*Doherty et al.*, 1999]. However, for supermicron homogeneous spheres,

Table 2a. PSAP Noise: Filtered Air and Parallel Measurements[a]

Test	Parameter	All	Level[b]	Δ Altitude[c]
A_{tot}	$\delta_{N,30}$ (Mm^{-1})	2.83	2.05	4.04
A_{tot}	(count)	(1445)	(870)	(153)
A_{sub}	$\delta_{N,30}$ (Mm^{-1})	1.80	0.94	2.95
A_{sub}	(count)	(3389)	(2081)	(961)
Parallel[d]	$\delta_{N,30}$ (Mm^{-1})	2.78	1.76	4.10
Parallel[d]	(count)	(1523)	(903)	(467)

[a]Results from filtered air measurements spanning all flights but concentrated on flights 1−5. $\delta_{N,30}$ indicates noise (2 SD) at 30-s time resolution and count indicates the number of data points analyzed.

[b]This column shows $\delta_{N,30}$ and count data for level altitude periods (dz/dt < 1 m s^{-1}).

[c]This column shows $\delta_{N,30}$ and count data for changing altitude periods (dz/dt > 2 m s^{-1}).

[d]For instruments operated in parallel, reported noise is twice the root-mean square discrepancy.

Mie theory predicts a significant difference between the two quantities because of resonance in the scattered wave fronts. Hydrated sea salt fits this description and requires a significant correction, as shown by *Masonis et al.* [2003]. However, sea salt was a minor contributor to the light scattering measurements in this campaign and, in any case, nearly all β_p measurements were made at RH< 40% where sea salt is largely crystallized [*Tang*, 1997]. Thus super-micron particles measured by N_{180} in this campaign (mineral dust, fly ash, and crystallized sea salt) are expected to be highly nonspherical and not subject to the resonant phenomena Mie theory predicts in the vicinity of 180°For perfect spheres. Given this, we expect the difference between 177° and 180° backscatter to be small and, for the present study, we make no correction.

2.3.3. PSAP Data Reduction

[28] The PSAP measurements of σ_{ap} were corrected for flow rate calibrations, filter spot size, instrument calibration bias, and scattering artifact according to the recommendations of *Bond et al.* [1999]. Built into these corrections is an adjustment from the instrumental wavelength of 565 nm to 550 nm. To allow improved smoothing (noise reduction), this approach was applied to the PSAP's signal (S) and reference (R) voltages. In short, σ_{ap} (Mm^{-1}) at 550 nm was calculated as follows,

$$\sigma_{ap} = \left[\frac{C}{mTr + n} \frac{A}{Qdt} \ln\left(\frac{S_p/R_p}{S/R} \right) - K_1 \sigma_{sp,raw} \right] \frac{1}{K_2} \quad (9)$$

where C is a constant (set to 6×10^4 to account for the division of filter area by sample volume and to make the units of σ_{ap} come out in Mm^{-1}), m and n are constants established by the manufacturer's calibration (set to 1.0796 and 0.710, respectively), Tr is the relative filter transmission reported by the PSAP, A is the measured spot area on the filter (18.4 mm^2 for both units used in herein), Q is the calibrated volume flow rate (monitored with a mass flowmeter and maintained close to 1 L min^{-1} herein), dt is the time interval between readings (in minutes), S_p and R_p are the signal and reference voltages from the previous time step, K_1 and K_2 are the scattering and calibration correction factors determined by *Bond et al.* [1999] (set to 0.02 ± 0.02 and 1.22 ± 0.2, respectively), and $\sigma_{sp,raw}$ is the nephelometer-measured scattering coefficient at 550 nm (Mm^{-1}). (The subscript "raw" means preangular correction. Using

raw scattering is important for coarse mode aerosols where near-forward scattering becomes dominant. This component of scattering is not sensed by a nephelometer and also is not thought to contribute to the PSAP scattering artifact.)

[29] The PSAP provides S and P readings every second, but data at this resolution are much too noisy to be useful. We found that a running, 30-s average eliminated most of the high frequency noise while preserving essentially all of the meaningful information. This is evident in Figures 3g and 3h, which show the response to a step change in concentration for both 5-s and 30-s smoothed data. Moreover, we found that averaging the S and R values prior to calculating σ_{ap} produced a less noisy result than doing the averaging after calculating σ_{ap}.

2.4. Noise, Precision, and Artifact Tests

[30] An understanding of instrumental noise is critical to any assessment of variability. Knowledge of precision is required in order to judge whether measured differences are robust. Previous studies have not carefully examined the performance characteristics of nephelometers and PSAPs on aircraft. The PSAP, in particular, is known to respond to pressure and RH changes, but these effects have not previously been quantified. This section describes our efforts at such quantification. Noise and precision measurements are shown in Figure 5 and Tables 2a, 2b, and 3. An example of an RH-induced PSAP artifact is shown in Figure 6 and a correction scheme will be suggested (section 2.4.2). A systematic discrepancy between light scattering measurements by the TSI and Radiance Research nephelometers is shown in Figure 7 and discussed in section 2.4.3.

2.4.1. Nephelometer Noise and Precision Measurements

[31] A nephelometer senses light scattered by particles, gas molecules and internal wall surfaces, but the latter two are subtracted away based on a priori knowledge of air scattering (as a function of air density, which is monitored) and the calibration procedure. Thus, in the absence of particles, a nephelometer should read zero and deviations from zero are a direct measurement of calibration error (the systematic part of the deviations; see section 2.3.1) and instrumental noise (the random part). Noise measurements were obtained on every flight by routinely setting the rack-zeroing valve to the filtered air position. These data provide baseline noise levels for predicting noise as a function of

Table 2b. Tests With Clean Versus Dirty Glass-Fiber Filter in Optical Sensing Block[a]

Test	Parameter	All	Level[b]	Δ Altitude[c]	ΔRH[d]
Clean	$\delta_{N,30}$ (Mm^{-1})	0.52	0.26	0.78	1.45
Clean	(count)	(1066)	(581)	(344)	(25)
Dirty	$\delta_{N,30}$ (Mm^{-1})	2.89	1.10	5.63	8.57
Dirty	(count)	(1010)	(687)	(222)	(72)

[a]Results from filtered air measurements spanning all flights but concentrated on flights 1−5. $\delta_{N,30}$ indicates noise (2 SD) at 30-s time resolution and count indicates the number of data points analyzed. Data are from the A_{sub} PSAP exclusively.

[b]This column shows $\delta_{N,30}$ and count data for level altitude periods (dz/dt < 1 m s^{-1}).

[c]This column shows $\delta_{N,30}$ and count data for changing altitude periods (dz/dt > 2 m s^{-1}).

[d]This column shows $\delta_{N,30}$ and count data for changing RH periods identified by hand in the vicinity of the top of the marine boundary layer.
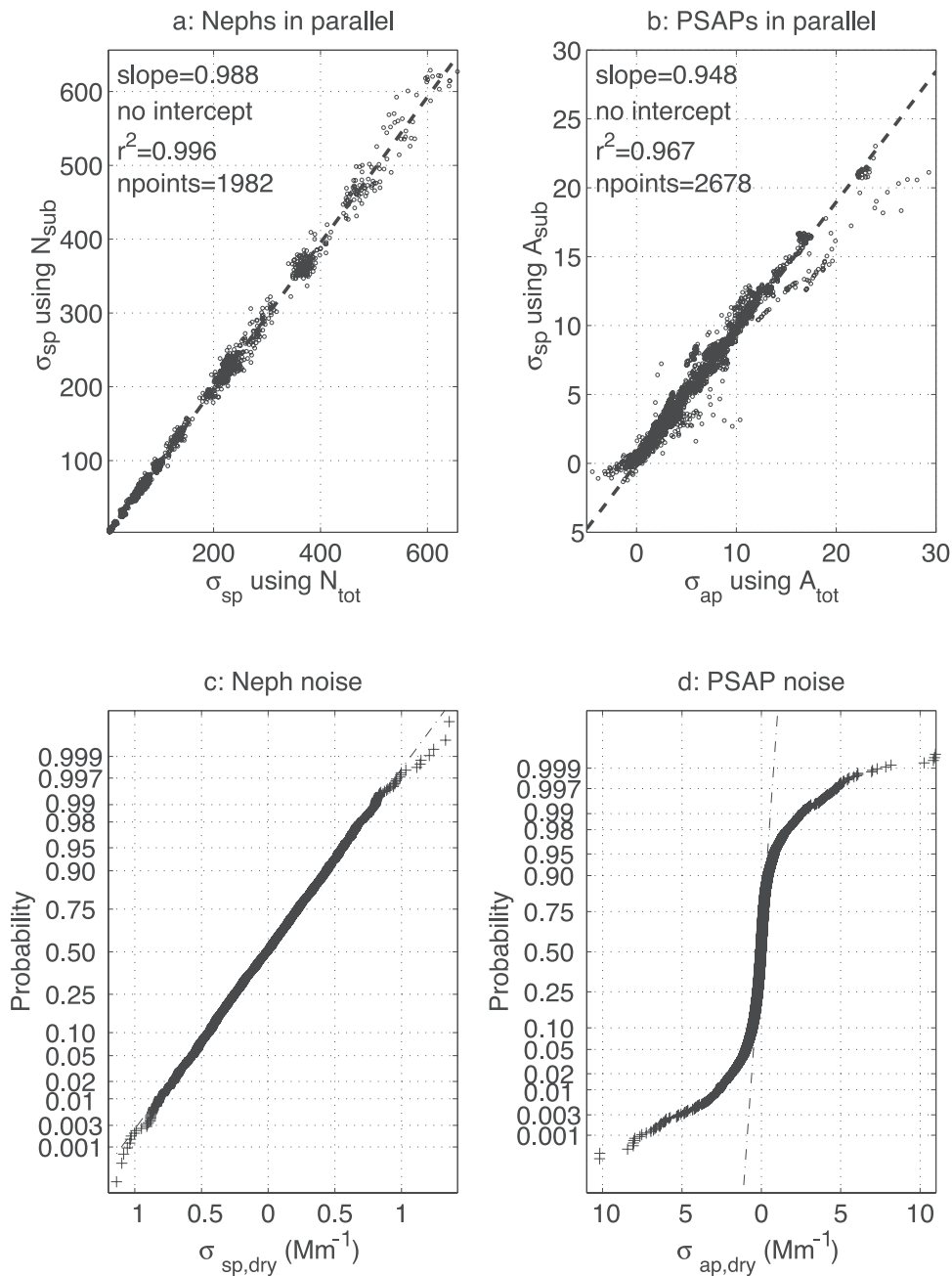
a: Nephs in parallel

slope=0.988
no intercept
r^2=0.996
npoints=1982

b: PSAPs in parallel

slope=0.948
no intercept
r^2=0.967
npoints=2678

c: Neph noise

d: PSAP noise

Figure 5. In-flight measurements of precision and noise. Scattering and absorption measurements with units in parallel (a and b) or while measuring filtered air (c and d). (a) All data at 2-s time resolution for $\sigma_{sp}(550)$ from times when both the N_{tot} and N_{sub} nephelometers were measuring the total aerosol. A 2% systematic discrepancy is indicated and the random discrepancy (noise) is seen to increase with scattering magnitude. (b) All data at 30-s time resolution for $\sigma_{ap}(550)$ from times when both the A_{tot} and A_{sub} PSAPs were measuring the total aerosol. A 5% systematic discrepancy is indicated and the random discrepancy (noise) has no detectable dependence on the magnitude of the absorption coefficient. (c) Cumulative, log-probability distribution of all $\sigma_{sp}(550)$ filtered air measurements taken with the N_{sub} nephelometer. (d) Same as Figure 5c but for the A_{sub} PSAP. Nephelometer noise is seen to be normally distributed while the upper and lower 10% of PSAP noise data deviates strongly from normal.

scattering level and averaging time (see section 2.5 and Table 3).

[32] Several additional tests provide further insights into the nature of nephelometer noise. First, we calculated the ratio of noise measured during altitude changes to noise measured during level flight legs. This ratio is never greater than 1.1 for any of the nephelometer measurements, showing a negligible effect. Because altitude changes are commonly associated with rapid changes in ambient RH, these data indicate insensitivity to RH changes as well. Second, filtered air measurements by one of the nephelometers, N_{sub}, are shown in Figure 5c to be normally distributed to a very

Table 3. Uncertainty Parameters for Computing Precision of Level-Leg Averages

Instrument	Measurement	σ_{air}(STP), Mm^{-1}	W, Mm^{-1}	$\delta_{N,240}$, Mm^{-1}	P_{sys}
N_{tot}	$\sigma_{sp,dry}$ (450)	27.61	4.08	0.37	0.046
N_{tot}	$\sigma_{sp,dry}$ (550)	12.125	3.98	0.15	0.012
N_{tot}	$\sigma_{sp,dry}$ (700)	4.459	6.16	0.14	0.035
N_{tot}	$\sigma_{bsp,dry}$ (450)	13.805	1.13	0.26	0.012
N_{tot}	$\sigma_{bsp,dry}$ (550)	6.0625	1.12	0.10	0.018
N_{tot}	$\sigma_{bsp,dry}$ (700)	2.2745	2.30	0.12	0.012
N_{sub}	$\sigma_{sp,dry}$ (450)	27.61	3.04	0.34	0.046
N_{sub}	$\sigma_{sp,dry}$ (550)	12.125	3.21	0.14	0.012
N_{sub}	$\sigma_{sp,dry}$ (700)	4.459	4.89	0.14	0.035
N_{sub}	$\sigma_{bsp,dry}$ (450)	13.805	1.86	0.25	0.012
N_{sub}	$\sigma_{bsp,dry}$ (550)	6.0625	1.78	0.10	0.018
N_{sub}	$\sigma_{bsp,dry}$ (700)	2.2745	2.63	0.13	0.012
N_{dry}	$\sigma_{sp,dry}$ (540)	13.05	6.5	0.46	0.02
N_{wet}	$\sigma_{sp,wet}$ (540)	13.05	6.5	0.58	0.03
A_{tot}	$\sigma_{ap,dry}$ (550)	n/a	n/a	0.72	0.05
A_{sub}	$\sigma_{ap,dry}$ (550)	n/a	n/a	0.33	0.05
N_{180}	$\beta_{180,dry}$ (532)[a]	1.6322	0.12	0.007	0.02
RH for N_{wet}	RH[b]	n/a	n/a	1%	1%

Columns are σ_{air}(STP): scattering coefficient of air at 273.2K and 1013.2 mb; W: nephelometer wall scattering; $\delta_{N,240}$: noise at 240 s time resolution (random instrumental error); P_{sys}: systematic component of precision uncertainty.

[a]Units for β_{180} are Mm^{-1} sr^{-1}.
[b]Units for RH are %RH.

good approximation. Finally, the two TSI nephelometers, N_{tot} and N_{sub}, were operated in parallel many times during the campaign (by simply bypassing the 1-μm impactor in front of N_{sub}). This test permits noise and precision to be assessed during actual particle-scattering measurements. Figure 5a displays the resulting data for σ_{sp}(550) at 2-s resolution. The systematic discrepancy (slope of the regression) is less than 2%. The point-by-point error is seen to increase steadily with scattering magnitude, consistent with the recommended model [*Anderson et al.*, 1996] of Poisson distributed photon-counting noise. (An examination of the residuals showed that 41% of the variance was associated with scattering magnitude.) These results confirm and extend the findings of previous ground-based studies [*Anderson et al.*, 1996; *Anderson and Ogren*, 1998] that nephelometer noise is normally distributed, independent of altitude or RH changes, and predictably dependent on sample time and scattering magnitude.

2.4.2. PSAP Noise, Precision, and Artifact Measurements

[33] Submicron absorption measurements were sacrificed during the first five flights in order to study noise and artifact aspects of the PSAP. To accomplish this, the "A_{sub}" PSAP sampled from N_{tot} (rather than N_{sub}) during these flights and thus sampled in parallel with the A_{tot} PSAP. Duplicate absorption measurements, which allow instrumental noise as a function of signal magnitude to be studied by examining the discrepancy between the two units, were obtained during parts of RF01 and all of RF04 and RF05. For two other flights (RF02 and RF03) the A_{sub} PSAP sampled particle-free air by means of an in-line filter placed at the PSAP inlet. This allowed noise and artifacts occurring during pressure and RH changes to be thoroughly studied. Because RH artifacts are expected to vary with particle loading on the internal PSAP filter, this filter was heavily loaded with particles (light transmission relative to a clean

filter = 0.74) for RF02 and was clean (transmission = 1.00) for RF03. Both the A_{sub} and A_{tot} PSAPs were operated in this particle-free sample mode during large portions of RF01.

[34] Results of these studies are summarized in Table 2. Comparing the rows in Table 2a shows that the A_{tot} unit was noisier than the A_{sub} unit (consistent with the leak information above) and that the parallel tests gave noise levels comparable to A_{tot}. Since the parallel tests examined the discrepancy between units during actual measurements of particle absorption, this result shows that PSAP noise does not depend on the magnitude of σ_{ap}. This follows logically from fact that the PSAP responds to a relative measurement (ratio of light transmission through a sample versus a reference filter) rather than to an absolute measurement. (The nephelometer, in contrast, responds to an absolute measurement - photon counts.) Comparing the columns of Table 2a shows that PSAP noise is considerably greater for changing altitude conditions than for level-leg conditions.

[35] Sensitivities to particle loading on the PSAP internal filter are shown in Table 2b. These results apply to the A_{sub} instrument only. Noise for the "dirty" filter is seen to be about 5 times higher than for the "clean" filter. For a clean filter on level flight with a well-sealed PSAP, noise is quite modest (0.3 Mm^{-1} for 30 s time resolution.) This same PSAP displays noise levels of almost 9 Mm^{-1} when operated with a dirty filter and exposed to rapid RH changes. Note that instrumental RH in these tests was never above 50%, so this is not a matter of particles deliquescing on the filter. Rather, humidity changes, even at low RH, effect light transmission through the PSAP filter, especially when it is loaded with particles. These changes in light transmission are actually quite subtle. For the flow rate and time resolution used, a relative change in transmission of 10^{-6} corresponds to an apparent σ_{ap} of roughly 1 Mm^{-1}.

[36] An example of an RH-induced artifact is shown in Figure 6. Data from an ascent through a strong gradient in ambient RH are displayed. Data are from RF02, so the A_{sub} PSAP was measuring particle-free air and its internal filter was "dirty". Figure 6a shows that both PSAPs responded to the changing RH, first with a negative artifact (e.g., at 900 m altitude), then with a positive artifact (e.g., at 1400 m.) A reasonable case can be made that aerosol intensive properties were in fact constant between 600 and 2000 m, as evidenced by the measurements of FF$_{scat}$ (Figure 6b). Thus a correction scheme can be employed wherein ω in the artifact region is set to the measured value from an adjacent region that (1) appears to have a valid σ_{ap} measurement and (2) appears to have comparable FF$_{scat}$. In the example shown, an ω value of 0.90 can be obtained from the region between 1800 and 2000 m. This scheme allows for the removal of obvious, RH-induced artifacts in vertical profiles of σ_{ap}; however, it is somewhat tedious in that each profile must be examined and corrected by hand.

2.4.3. Radiance Research Versus TSI Nephelometers: An Enigma

[37] Measurements of mid-visible σ_{sp} at low RH by N_{tot} and N_{dry} represent replicate measurements using two different models and styles of nephelometer - the TSI model 3563 and the Radiance Research (RR) model M903, respectively. Figure 7 shows that the RR nephelometer measures consistently lower than the TSI. The discrepancy
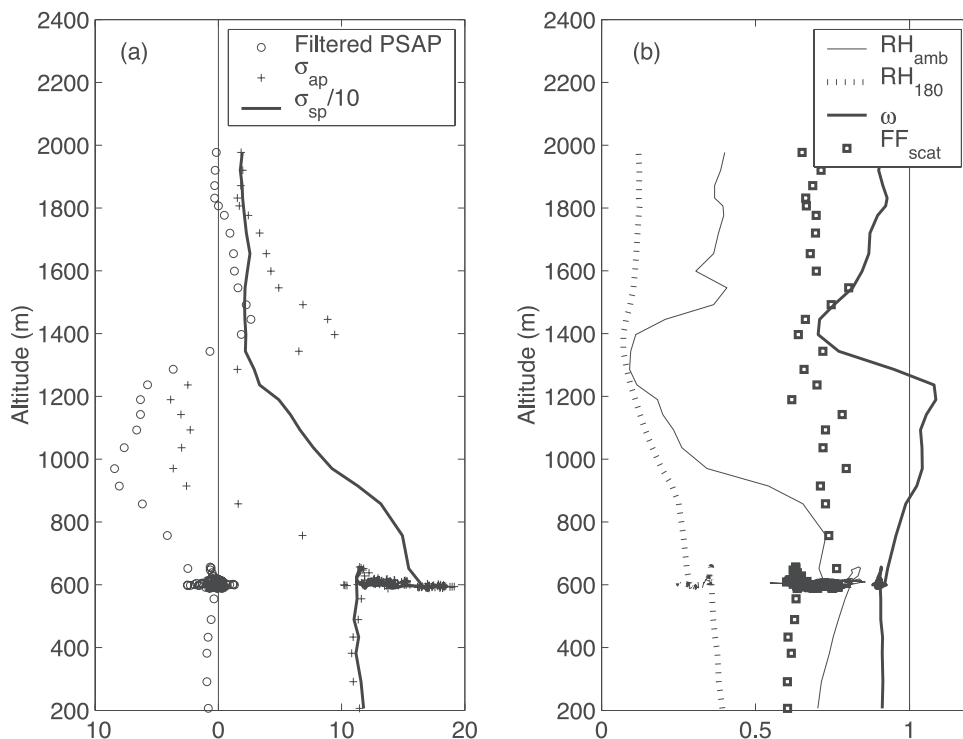
Figure 6. Profiles of light absorption, light scattering, and single-scattering albedo during an ascent out of the boundary layer and through a large gradient in ambient RH. Data are from research flight 2, 2 April 2001, at 0130 UTC. One PSAP (circles in Figure 6a) sampled particle-free air. The break in the profile of aerosol concentration at 600 m is associated with 70 km long horizontal transect at this elevation. Nonphysical PSAP measurements are indicated when σ_{ap} goes below zero (Figure 6a) or ω goes above 1 (Figure 6b.) These occur in association with the large drop in both ambient and instrumental RH between 800 and 1300 m. (Note that the 180-nephelometer was immediately upstream of both PSAPs such that RH_{180} best reflects RH inside the PSAP. The latter was not directly measured.) A corresponding positive artifact is evident at around 1400 m. Evidence that aerosol intensive properties are in fact rather constant with altitude from 600 to 2000 m is provided by measurements of FF_{scat} (Figure 6b). This is the basis for a manual correction scheme described in the text.

is modest (about 10%) when submicron particles dominate the scattering but becomes quite substantial (about 30%) when supermicron particles dominate. Subsequent to the field campaign, laboratory studies were undertaken to explore this effect, using the identical two instruments. These revealed (1) the discrepancy can be reproduced using white powder (zinc strearate) that, like mineral dust, is irregularly shaped and primarily supermicron in size, (2) the discrepancy cannot be explained by plumbing losses of large particles, and (3) the RR nephelometer has a somewhat higher forward truncation angle (10° versus 7° for the TSI), but this by itself only explains about one third of the effect. We tentatively conclude therefore that most of the discrepancy is due to the angular distribution of light in the RR nephelometer, which is not presently known. (To explain the effect, the illumination intensity would have to be positively biased in the 90° scattering region and negatively biased in the forward scattering region.) Measurement of this angular distribution is therefore an important future research topic. These measurements should include illumination of the sensing volume by reflection off the wall immediately opposite to the flash lamp.

[38] For the present study, measurements by the RR nephelometers were only used in a relative sense, i.e., to determine f_{RH} (equation (5)). Any attempt to correct the data would require knowledge of the humidity dependence of the correction, which we do not have. Therefore we make no correction. In effect, we are assuming that f_{RH} can be determined accurately from a less-than-ideal measurement of total scatter, as long as the total scatter measurement is made consistently in both the high and low RH devices. We have attempted to fulfill this requirement by using identical nephelometers and carefully matching the flow paths to each instrument in terms of flow rate, tubing diameters, and sharpness of bends.

2.5. Uncertainty Estimation

[39] As described above, the determination of optical properties involves a sequence of steps beginning with the raw data and including instrument calibrations as well as various adjustments and corrections. For each of these steps we have developed an uncertainty estimate that reflects the potential for error at the 95% confidence level, as explained in previous publications [*Anderson et al.*, 1996, 1999, 2000; *Anderson and Ogren*, 1998; *Bond et al.*, 1999; *Doherty et al.*, 1999]. Here we extend this approach to airborne measurements and to the Radiance Research nephelometer. We focus on determining noise, precision and total uncer-
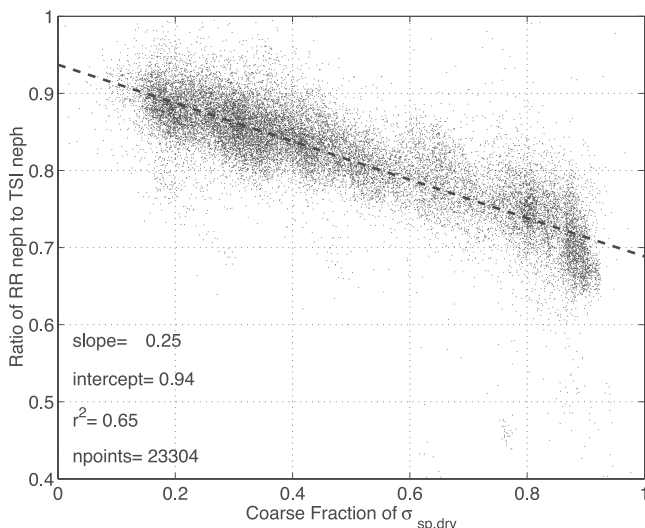
Figure 7. Ratio of midvisible light scattering measurement by the Radiance Research (RR) nephelometer (model M903) to that of the TSI nephelometer (model 3563), plotted as a function of the coarse-mode fraction of scattering $(1 - FF_{scat})$. For the purpose of this comparison, nephelometer data have not been corrected for angular truncation. The TSI data have been adjusted to the RR wavelength of 540 nm using the TSI measurements at 550 and 450 nm.

tainty of level-leg averages, as this will be the subject of the results section.

[40] Data during all level-leg portions of all flights were averaged into separate "samples" of 4 to 35 min in length. Statistical properties of this sample population will be presented in section 3. How well can we determine the average and standard deviation over a set of such samples? To address this, we calculate three types of uncertainty: noise, precision, and total uncertainty.

[41] We estimate the noise per level-leg sample, $\delta_{N,leg}$, in order to judge whether the measured variability among samples is significant. Noise scales with the square root of sample time. Since each level-leg sample is at least 4 min (240 s) long, we adopt the conservative convention of using the estimated noise for 240-s averaging, $\delta_{N,240}$, for all legs. Table 3 shows the values of $\delta_{N,240}$ for each instrument as determined by the filtered air measurements. In the case of the PSAPs, the "Level" data from Table 2a have been used as a starting point. Noise for the nephelometers also scales with scattering magnitude. For a given category of level-leg samples, we calculate $\delta_{N,leg}$ using the average scattering value over that category, $\langle \sigma_{sp} \rangle$,

$$\delta_{N,leg} = \delta_{N,240} \sqrt{\frac{(\langle \sigma_{sp} \rangle + \sigma_{air} + W)}{\sigma_{air} + W}} \qquad (10)$$

where σ_{air} is the scattering due to air and W is the so-called "wall-scattering", or the artifact scattering due to reflection off internal surfaces within the nephelometer. Table 3 gives σ_{air}(STP) and W for each nephelometer parameter. (The former must be adjusted for actual air density inside the nephelometer.)

[42] We calculate the precision of the average of a set of level-leg samples, $\delta_{P,ave}$, in order to judge whether differences among categories of sample-types are significant. Precision means the expected discrepancy between identical instruments deployed in parallel or on separate occasions. It includes a random component (noise) as well as a systematic component, which we designate P_{sys}. The noise component is $\delta_{N,leg}$ (which applies to a single level-leg sample) divided by the square root of the number of legs that contribute to the average. Thus taking σ_{sp} as an example,

$$\delta_{P,ave} = \sqrt{\frac{\delta_{N,leg}^2}{N_{legs}} + \left(\langle \sigma_{sp} \rangle P_{sys} \right)^2} \qquad (11)$$

where N_{legs} is the number of samples contributing to the average. For the standard TSI nephelometers and the PSAPs, precision was measured directly via parallel operation of pairs of identical instruments. Sample results are shown in Figures 6a and 6b. Table 3 shows the values of P_{sys} for each instrument. For the TSI nephelometers and PSAPs, these values come from direct measurements. For the Radiance Research nephelometers, N_{dry} and N_{wet}, and for the 180-nephelometer, N_{180}, we estimate P_{sys} from the calibration stability data obtained via filtered air measurements.

[43] We calculate total uncertainty of the average, $\delta_{U,ave}$, as the quadratic sum of $\delta_{P,ave}$ and all other known sources of measurement uncertainty. Thus for a given measured quantity, $\delta_{U,ave}$ refers to the estimated overall accuracy of the average. This is the appropriate uncertainty to use when comparing our measurements to independent measurements of the same quantity (closure tests) and for model- and satellite-validation activities. Additional uncertainty components that enter in to total uncertainty are (1) estimated method accuracy derived from laboratory closure experiments, set to 7% for the standard TSI nephelometers [*Anderson et al.*, 1996] and the 180-nephelometer [*Anderson et al.*, 1999] and 20% for the PSAPs [*Bond et al.*, 1999], (2) nephelometer calibration accuracy derived from multiple calibrations over the campaign using the approach of *Anderson and Ogren* [1998], (3) uncertainty of the nephelometer correction for angular nonidealities, derived from Mie calculations, using the formulas recommended by *Anderson and Ogren* [1998], (4) uncertainty of the PSAP scattering correction, set to ±50% of the correction, and (5) uncertainty of the various wavelength and RH adjustments, set to ±50% of the corrections. In addition, in view of the possible sampling bias for coarse mode aerosol introduced by the Low Turbulence Inlet and sample plumbing (see Figure 4), we assign an additional 10% uncertainty to all supermicron scattering and absorption measurements.

[44] All uncertainties are assumed to be independent and are therefore added in quadrature. Uncertainties of intensive properties are calculated by standard propagation of errors, using the derivatives of equations (1)–(7), above, with respect to each extensive property. This assumes linear behavior, an assumption that breaks down in the case of aerosol hydration with respect to errors in the measurement of RH. Therefore for f_{RH} we use uncertainties in all the input parameters to calculate maximum and minimum values, then take half the difference between these extremes as the estimated uncertainty. The high RH measurement is by far the most important source of uncertainty in determining f_{RH}.

RH was measured both at the inlet and outlet of N_{wet}. The noise and precision uncertainties given in Table 3 are based on variations in the difference between these two sensors. Since some of these variations are real, this is probably an overestimate. For estimating total uncertainty, we adopt the manufacturer's stated accuracy of ±3.5% RH at 85% RH. On the basis of repeated RH calibrations during the campaign and the use of dual sensors, this, too, seems to be conservative, but is intended to encompass the possibility that RH inside the nephelometer may have differed slightly from the average of the upstream and downstream measurements.

3. Results

[45] While other papers in this issue focus on case studies and characterization of the vertical column [e.g., *Redemann et al.*, 2003], we pursue a statistical overview of the measured aerosol optical properties encountered throughout the campaign by the C-130 aircraft. For this purpose, we obtain a set of quasi-independent samples with minimal instrumental noise by averaging over all the level-leg portions of each flight. "Level" flight was defined as ascent or descent rates less than 1 m s^{-1}. At least 2 min of level flight were required before beginning a sample and samples had to be at least 4 min long to be used. 244 legs meeting these criteria were identified. All legs longer than ~30 min were split into 2 or more samples, based on an earlier study of this same data set [*Anderson et al.*, 2003] that found considerable variation for offset distances larger than 90 km (the distance traversed in 15 min). In all, 299 samples were identified. However, not all properties were measured during each sample such that individual correlations and statistics presented below are based on subsets of these 299 samples. The remainder of this paper consists of an analysis of these samples.

3.1. Statistical Summary of Aerosol Optical Properties and Uncertainties

[46] The level-leg samples have been separated into 8 categories, as shown in Table 4 and explained in more detail below. For each category, 8 optical properties are quantified. These divide into three extensive properties and five intensive properties. The extensive properties were selected to represent the three main types of instruments: $\sigma_{sp}(550)$ (standard nephelometer), σ_{ap} (PSAP), β_p (180-nephelometer). The intensive properties, which were defined in section 1, are key parameters needed to calculate aerosol radiative effects. Therefore it is of interest to know not only the average values that derive from our measurements but also how well our measurements serve to constrain these values. For each property and category, Table 4 shows the number of level-legs that were available for analysis (N_{legs}), the average (Ave) and standard deviation (SD) calculated by treating each level-leg as an independent sample, the precision with which the average could be determined ($\delta_{P,ave}$), the total uncertainty of the average ($\delta_{U,ave}$), and the ratio of the measured standard deviation to the measurement noise per level-leg sample (SD/$\delta_{N,leg}$).

[47] The uncertainty-related parameters can be interpreted as follows. $\delta_{P,ave}$ allows assessment of whether differences between categories are significant either within this study or when compared to other field campaigns using the same instrumentation. $\delta_{U,ave}$ allows assessment of

whether properties measured herein are significantly different from properties measured with different instrumentation. SD/$\delta_{N,leg}$ allows assessment of whether the measured standard deviation represents true variation or instrumental noise - for the former to be true, this ratio should be larger than 2, as it is in most cases shown.

[48] The SD/$\delta_{N,leg}$ parameter also allows the variability of extensive and intensive parameters to be directly compared, since instrumental noise provides a consistent normalization. The extreme possibilities are as follows: (1) if extensive parameters varied completely independently of each other, SD/$\delta_{N,leg}$ would be similar for both extensive and intensive parameters, whereas (2) if intensive parameters were truly invariant (extensives perfectly correlated), SD/$\delta_{N,leg}$ would be unity for all the intensive parameters. The latter would occur, for example, if all variation were due to variable dilution. Table 4 shows that SD/$\delta_{N,leg}$ is often about 10 times greater for the extensive than for the intensive properties, indicating that the extensives are far more variable than the intensives. Nevertheless, some variation of the intensive properties is detectable. From the point of view of a satellite retrieval or a chemical transport models that assumes fixed intensive properties, this variation represents a source of methodological uncertainty.

3.2. Aerosol Categories

[49] Arguably, the most basic aerosol categorization strategy is the separation of mechanically produced coarse mode material (primarily dust, sea salt, and organic debris) from combustion- and oxidation-derived fine mode material (primarily sulfates, organics, and black carbon). This strategy follows from the discovery more than 30 years ago of the bimodal distribution of aerosol mass [*Whitby et al.*, 1972]. The technique of separately analyzing the optical properties of these two modes via inertial separation was pioneered by *White et al.* [1994]. Coarse/fine separation has proven to be a powerful technique for understanding aerosol optical properties in many regions. Here we test how well this approach applies to the aerosol in the Asian outflow region.

[50] The first three categories in Table 4 show the statistics for the entire set of level-leg samples, first for the total aerosol then for the submicron and supermicron portions of the aerosol, respectively. Note that submicron and supermicron particles make roughly equal contributions to mid-visible light extinction according to this analysis. That is, the average low RH light extinction at 550 nm by the submicron aerosol (36.2 Mm^{-1}) is 66% that of the supermicron aerosol, and this deficit is largely balanced by the fact that the submicron aerosol is considerably more hygroscopic (f_{RH} is 1.7 versus 1.3 for the supermicron aerosol). The intensive properties of these two categories are distinctly different in some respects. Submicron å is much higher; however, this follows inevitably from the difference in particle size. Submicron b is significantly higher, which also could be explained simply due to the difference in size. Reflecting differences in chemical composition are the facts that single scatter albedo is much lower and hygroscopicity much higher for the submicron aerosol. Note that β_p and S cannot be determined for the submicron and supermicron categories since we made no submicron measurement of β_p.

[51] The next three categories in Table 4 examine the total aerosol but separate the level-leg samples in terms fine-mode fraction, FF_{scat} (equation (1)). Figure 8 shows that the level-leg samples spanned a wide range of FF_{scat}, from

Table 4. Values and Uncertainties of Optical Properties for Aerosol Categories[a]

	Extensive Properties			Intensive Properties				
	σ_{sp}, Mm^{-1}	σ_{ap}, Mm^{-1}	β_p, $Mm^{-1} sr^{-1}$	å	b	ω	f_{RH}	S, sr
All (All Cases, Total Aerosol)								
N_{legs}	299	299	299	277	178	237	212	237
Ave	83.3	7.0	2.04	0.90	0.124	0.923	1.51	45.8
$\delta_{P,ave}$	1.0	0.4	0.04	0.13	0.005	0.004	0.09	1.0
$\delta_{U,ave}$	11.4	1.5	0.15	0.46	0.019	0.018	0.15	6.5
SD	100.6	8.3	2.44	0.53	0.015	0.032	0.32	9.4
$SD/\delta_{N,leg}$	270	12	166	25	5	4	5	19
Submicron (All Cases, Submicron Portion)								
N_{legs}	298	224	–	208	94	129	40	–
Ave	30.6	5.6	–	1.91	0.149	0.846	1.67	–
$\delta_{P,ave}$	0.4	0.3	–	0.13	0.005	0.007	0.11	–
$\delta_{U,ave}$	2.6	1.2	–	0.34	0.016	0.029	0.21	–
SD	32.4	6.1	–	0.42	0.020	0.043	0.30	–
$SD/\delta_{N,leg}$	134	19	–	10	2	6	4	–
Supermicron (All Cases, Supermicron Portion)								
N_{legs}	298	224	–	253	105	170	30	–
Ave	52.7	2.2	–	0.13	0.117	0.972	1.28	–
$\delta_{P,ave}$	1.3	0.2	–	0.26	0.009	0.004	0.12	–
$\delta_{U,ave}$	10.5	0.5	–	0.71	0.023	0.011	0.15	–
SD	86.8	4.1	–	0.20	0.015	(0.021)	0.29	–
$SD/\delta_{N,leg}$	195	5	–	4	3	1.5	2.8	–
Fine Dominated (Cases With FF_{scat} > 0.6, Total Aerosol)								
N_{legs}	74	74	74	74	56	70	65	70
Ave	78.4	8.8	1.81	1.51	0.124	0.897	1.75	50.1
$\delta_{P,ave}$	0.9	0.5	0.04	0.13	0.005	0.005	0.12	1.1
$\delta_{U,ave}$	7.1	1.8	0.13	0.32	0.015	0.020	0.24	5.4
SD	47.5	5.2	1.18	0.20	0.015	0.020	0.20	10.1
$SD/\delta_{N,leg}$	131	7	83	9	4	2.7	2.3	17
Mixed (Cases With 0.3 < FF_{scat} < 0.6, Total Aerosol)								
N_{legs}	91	91	91	91	51	66	59	66
Ave	62.8	6.5	1.65	1.02	0.130	0.910	1.62	42.4
$\delta_{P,ave}$	0.8	0.3	0.03	0.13	0.005	0.005	0.10	1.0
$\delta_{U,ave}$	7.5	1.3	0.12	0.40	0.018	0.020	0.18	5.5
SD	61.4	6.9	1.46	0.24	0.012	(0.018)	0.20	8.7
$SD/\delta_{N,leg}$	185	10	105	9	3	1.9	2.5	14
Coarse-Dominated (Cases With FF_{scat} < 0.3, Total Aerosol)								
N_{legs}	93	93	93	93	65	90	78	90
Ave	134.9	8.9	3.24	0.30	0.121	0.948	1.22	46.5
$\delta_{P,ave}$	1.6	0.5	0.07	0.13	0.005	0.003	0.06	1.0
$\delta_{U,ave}$	23.2	1.8	0.24	0.57	0.021	0.016	0.08	7.9
SD	147.8	11.3	3.60	0.18	0.013	0.024	0.14	6.0
$SD/\delta_{N,leg}$	322	16	214	11	6	5	4	17
Pollution (Fine-Dominated, Submicron Portion)								
N_{legs}	74	40	–	71	45	34	16	–
Ave	55.3	8.6	–	2.10	0.141	0.876	1.73	(50)[b]
$\delta_{P,ave}$	0.7	0.4	–	0.13	0.005	0.006	0.12	–
$\delta_{U,ave}$	5.4	1.8	–	0.41	0.016	0.027	0.24	–
SD	34.0	4.7	–	0.16	0.018	0.030	0.20	–
$SD/\delta_{N,leg}$	113	14	–	6	3	7	2.3	–
Dust (Coarse-Dominated, Dust-Like Chemistry, Supermicron Portion)								
N_{legs}	30	26	–	30	28	26	7	–
Ave	212.2	8.8	–	0.02	0.121	0.964	1.06	(46)[b]
$\delta_{P,ave}$	5.1	0.9	–	0.26	0.009	0.004	0.09	–
$\delta_{U,ave}$	42.6	2.0	–	0.71	0.024	0.012	0.10	–
SD	161.2	7.3	–	0.08	0.008	0.013	0.16	–
$SD/\delta_{N,leg}$	248	9	–	5	5	4	5	–

below 0.1 to above 0.8. The distribution is fairly flat; however, if we examine only the high concentration cases (Figure 8b), the distribution becomes much more bimodal. We use this observation to establish the following categories: "coarse-dominated" (FF_{scat} < 0.3), "mixed" (0.3 < FF_{scat} < 0.6), and "fine-dominated" (FF_{scat} > 0.6). Divided in this way, the variability of most intensive properties is reduced (especially for the coarse-dominated cases), indicating that this categorization scheme captures something fundamental about the aerosol in this region. These categories are explored further in Figure 9, where box plots are used to show how leg altitude, aerosol hygroscopicity, and single scatter albedo are distributed for each category. Figure 9 makes an additional subdivision in terms of aerosol concentration: within each category, legs with $\sigma_{sp}(550)$ > 60 Mm^{-1} are separately analyzed. Figure 9a shows that coarse-dominated cases occurred throughout the lower troposphere, but fine-dominated cases, especially high concentration cases, occurred almost exclusively in the boundary layer. High concentration mixed cases were also confined to the boundary layer. Thus the outflow of fine-mode (presumably pollution) aerosol from the Asian continent occurred under meteorological regimes that inhibited lofting, while the coarse-mode aerosol (presumably dust) either originated at high altitude or was frequently lofted during transport. In terms of optical properties, Figure 9b shows that coarse-dominated and fine-dominated cases have almost nonoverlapping ranges in terms of hygroscopicity, while Figure 9c shows that their respective interquartile ranges do not overlap in terms of single scatter albedo. Thus a major portion of the observed variation in optical properties is captured by this categorization scheme.

[52] The final two categories in Table 4 represent an attempt to isolate the properties of the two dominate aerosol types observed in this campaign: fine-mode pollution and coarse-mode dust. They will be discussed in section 3.4.

3.3. Correlations Among Measured Parameters

[53] Our measurements yield a suite of 15 extensive optical properties: seven properties each (six scattering and one absorption) for the submicron and supermicron portions of the aerosol plus β_p, which was measured on the total aerosol only. Figure 10 examines the correlations among these parameters, specifically, the correlations of submicron $\sigma_{sp}(550)$ with all the others (Figure 10a) and the correlations of supermicron $\sigma_{sp}(550)$ with all the others (Figure 10b).

[54] Figure 10 shows that the supermicron parameters are essentially uncorrelated with the submicron parameters, and visa-versa. Figure 10a, parameters 8–14, exhibit r^2 values

Notes to Table 4

[a]Given are aerosol optical properties (defined in equations (1)–(7)) at low RH except for the humidity dependence of light scattering, f_{RH}. Parameters $\delta_{P,ave}$ and $\delta_{U,ave}$ are the 95% confidence precision and total uncertainties of the average. SD is the standard deviation over the individual legs that contribute to the average. $SD/\delta_{N,leg}$ is the standard deviation divided by the 95% confidence instrumental noise per level-leg sample. SD is highly uncertain and is thus shown in parentheses when this ratio is less than 2.

[b]Because fine/coarse separation was not made for the β_p measurement, the estimated lidar ratio, S, for the "Pollution" category is taken from the fine-dominated category and that for the "Dust" category is taken from the coarse-dominated category.

of about 0.1 indicating that only 10% of the variation in supermicron concentration is associated with variation in submicron concentration. Thus the two size classes are independent to a high degree. In part, this indicates that the choice of cut size used in this and many previous studies (1 μm aerodynamic diameter at low RH) is very effective at separating the coarse and fine modes in the Asian outflow region. More fundamentally, it shows that the bimodal model of atmospheric aerosol mass [*Whitby et al.*, 1972] applies in this region. (Exceptions to this description are discussed below.)

[55] Within each mode, the optical parameters are seen in Figure 10 to be highly correlated with each other. The six scattering parameters (numbered 1–6 and 8–13 for the submicron and supermicron modes, respectively) are so well correlated as to be almost interchangeable, while absorption is somewhat less well correlated, indicating a degree of independence from the rest. These high correlations indicate that the dominant source of variation is due to variation in aerosol amount, i.e., the extensive properties all tend to go up and down together, while the intensive properties are relatively invariant. (This is consistent with the difference in $SD/\delta_{N,leg}$ values for extensive versus intensive properties in Table 4.) Figure 11 explores the variation of intensive properties further. The left column of panels uses box plots to show the variability of å, b, and ω for the total, submicron, and supermicron aerosol. For these plots, the box represents the interquartile range (IQR), the whiskers represent a robust estimate of the total range, and the points outside the whiskers are estimated to be outliers. The IQRs never overlap between the submicron and supermicron aerosol, showing that the properties of these modes are quite distinct. Moreover, these IQRs are quite narrow, especially for the supermicron aerosol. The second and third columns explore causes for the full range of values. For the supermicron aerosol (right column) values outside the IQR
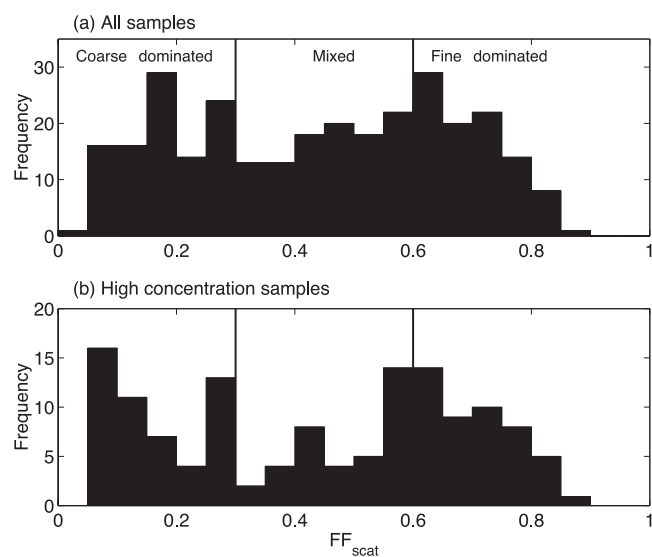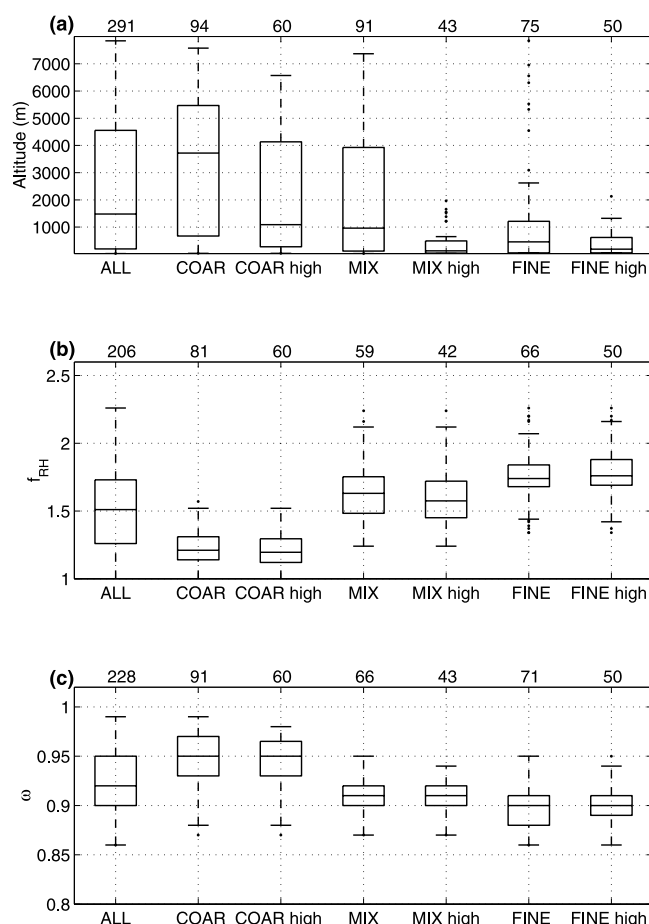

Figure 9. Distribution of selected properties for categories of level-leg samples. Categories are based on fine/coarse partitioning (COAR, coarse dominated; FINE, fine dominated; MIX, mixed, as discussed in the text), and the high-concentration samples ($\sigma_{sp}(550) > 60$ Mm^{-1}) for each category are separately displayed. Plots show the median (horizontal line), the interquartile range (IQR; box), an estimate of the full range (whiskers), and points estimated to be outliers (dots). A point that is outside of the IQR by more than 1.5 times the width of the IQR is considered an outlier. The number of samples in each distribution is shown at the top. The three panels show the distributions of points with respect to (a) altitude of the sample, (b) aerosol hygroscopicity, and (c) aerosol single scatter albedo.

Figure 8. Histogram of FF$_{scat}$ measurements during level-leg sampling. (a) All samples. (b) High-concentration samples, defined as $\sigma_{sp}(550) > 60$ Mm^{-1}. Vertical lines show divisions into aerosol categories used for subsequent analysis.

are seen to occur systematically at low concentration. Therefore it is likely that these reflect measurement noise and that the IQR is a good estimate of the true range of variation. This, in turn, implies that the intensive properties of the supermicron aerosol are very highly constrained over the course of this experiment. In contrast, for the submicron aerosol (middle column), Figures 11e and 11h show that values outside the IQR do not preferentially occur at low concentration and are thus likely to reflect real variation. Thus we conclude that the submicron aerosol is considerably more variable in terms of its intensive properties than is the supermicron aerosol.

[56] For Figure 11b the submicron values of å (y axis) are plotted, not against concentration, but against FF$_{scat}$. This
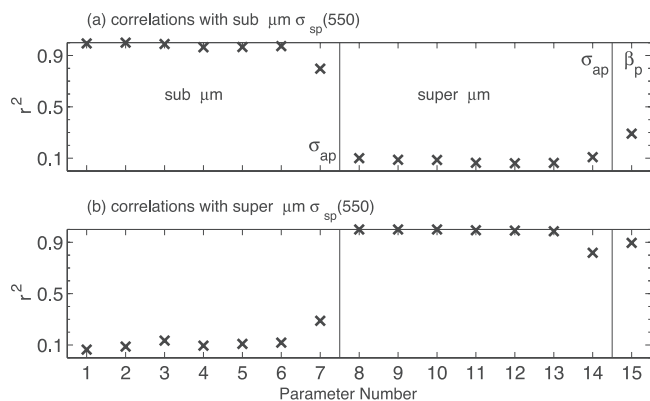
Figure 10. Correlations among parameters for the level-leg samples. Correlation coefficients (r^2) are shown for all 15 extensive optical properties when regressed against (a) submicron $\sigma_{sp}(550)$ and (b) supermicron $\sigma_{sp}(550)$. As indicated, the first seven parameters are submicron, the next seven are supermicron, and the final parameter is β_p, which was measured on the total aerosol only. The order of the submicron and supermicron parameters is σ_{sp} at 450, 550, and 700 nm, then σ_{bsp} at 450, 550, and 700 nm, then σ_{ap} at 550 nm. The submicron and supermicron portions of the aerosol are seen to vary independently.

reveals that the outliers arise entirely from cases in which the coarse-mode aerosol was highly dominant. There are two possible explanations. (1) The small particle tail of the coarse mode extended to sizes near and below the cut point. (Note that the impactor cut is not perfectly sharp. For example, particles with $D_{aero} = 1.12$ were sampled with approximately 30% efficiency [*Hillamo and Kauppinen*, 1991].) (2) Alternatively, some fraction of the coarse-mode particles may have bounced off the impactor substrate and therefore been measured by the submicron nephelometer, N_{sub}. We consider the latter to be unlikely, since the substrates were thoroughly greased to prevent bounce (although particle pile-up was considerable in some of the heavier dust events, which might possibly have caused some bounce.) The former explanation requires that particles with sizes near $D_{aero} = 1$ μm manifest values of å near zero; this is consistent with Mie theory. Therefore we take the result of Figure 11b as evidence that a small fraction of the coarse-mode mass exists near and below $D_{aero} = 1$ μm and that this fraction has a detectable influence on our measurement of submicron aerosol optical properties in cases where the coarse mode is dominant. In this sense, the two modes are not independent.

[57] There is a second way in which the submicron and supermicron aerosol appear to be linked. Whereas coarse-mode dust was frequently observed in almost pure form, fine-mode pollution was generally accompanied by a substantial coarse-mode component. For example, considering
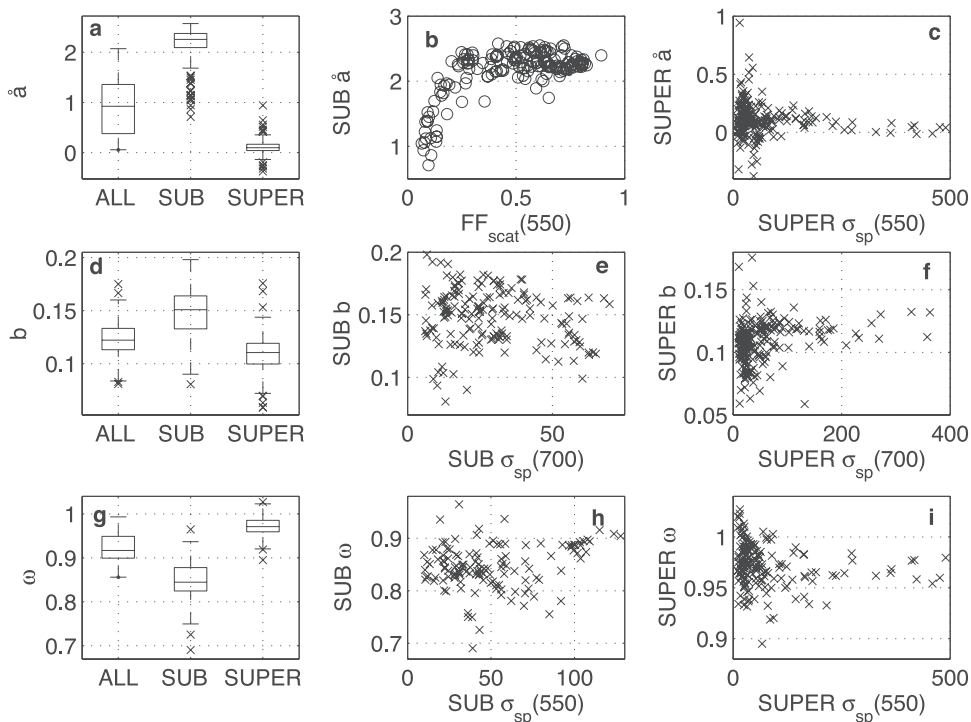

Figure 11. Consistency of intensive optical properties. Rows of panels display the variation of (a–c) å, (d–f) b, and (g–i) ω. These intensive properties are defined in equations (2), (3), and (4), respectively. Left column of panels shows the distribution of values using box plots for the total aerosol (ALL), the submicron aerosol (SUB), and the supermicron aerosol (SUPER). Box plot conventions are discussed in caption of Figure 9. Remaining panels show how the submicron (middle column) and supermicron (right column) values are distributed with respect to aerosol concentration, except Figure 11b, which shows how the submicron å data points are distributed with respect to fine-mode fraction, FF_{scat}.

the distribution of FF_{scat} for the high-concentration cases shown in Figure 8b, the most common type of coarse-dominated event had more the 90% of the scattering due to supermicron particles, while the most common type of fine-dominated event had only 60–75% of the scattering due to submicron particles. Thus it appears that coarse-mode aerosol is co-emitted with pollution aerosol in this region.

3.4. Optical Properties of "Pollution" and "Dust"

[58] The two dominant aerosol types observed during ACE-Asia were anthropogenic pollution and mineral dust. (Despite abundant measurements in the boundary layer over the ocean, rather little sea salt was observed, due to low wind speeds and, presumably, short residence times of most air masses in contact with the ocean surface.) The independence of submicron and supermicron aerosol components (Figure 10) is entirely consistent with the independent sources of these two aerosol types. Still, our measurements were made well downwind of the Asian continent where pollution and dust were generally intermingled to some extent. Here we attempt to disentangle them and offer a preliminary optical characterization of each one.

3.4.1. Pollution Properties

[59] Submicron, or fine-mode, aerosol is often a convenient proxy for anthropogenic pollution. However, mineral dust was pervasive during the ACE-Asia campaign and analysis herein (Figure 11b) indicates that the submicron tail of the dust size distribution did influence the submicron optical properties when dust was the dominant aerosol component. Therefore we estimate the optical properties of pollution aerosol in the Asian outflow region by examining the submicron portion of just the "fine-dominated" cases (i.e., level-leg samples with $FF_{scat} > 0.6$). Results are shown in Table 4 as the "Pollution" category. We find this aerosol to be moderately light-absorbing ($\omega = 0.88 \pm 0.03$; mean and 95% confidence uncertainty) and moderately hygroscopic ($f_{RH} = 1.7 \pm 0.2$).

[60] A curious feature of these data (not shown in Table 4) is that submicron ω is lower during the coarse-dominated events (at 0.82) than during the fine-dominated events (at 0.88). The precision of both these values is 0.01, indicating that the difference is real. Thus it appears that the submicron aerosol that accompanies dust plumes in this region is chemically distinct from (i.e., more absorbing than) both the dust itself and the typical pollution aerosol.

3.4.2. Dust Properties

[61] Dust events are easily recognized by low values of FF_{scat} combined with additional evidence that the coarse mode aerosol was not sea salt. Various types of indirect evidence were often available to indicate the absence of significant sea salt concentrations. These included observations that the sea surface was calm, that the coarse mode aerosol was not hygroscopic, that coarse mode concentrations did not increase toward the surface, and/or that the aircraft was flying above the boundary layer. Direct evidence on many occasions is provided by high values of the ratio of soluble Ca^{++} to soluble Na^+, both of which were measured with 4-min time resolution on the C-130 using a newly developed rapid ion chromatograph technique [*Weber et al.*, 2001]. The upper cut diameter for particles entering this device is estimated to be 1.3 μm, such that the sampled

aerosol was mostly the submicron tail of the coarse mode. We selected for analysis 30 cases from the level-leg sample set where (1) FF_{scat} was <0.3, (2) Ca^{++}/Na^+ (mass ratio) was >10, and (3) $\sigma_{sp,coar}$ was >45 Mm^{-1}. The properties of the supermicron aerosol for these cases are shown in Table 4 as the "Dust" category. The most striking properties are high single scatter albedo ($\omega = 0.964 \pm 0.012$; mean and 95% confidence uncertainty) and low hygroscopicity ($f_{RH} = 1.1 \pm 0.1$).

[62] Note that for the "Supermicron" category of Table 4, ω was somewhat higher (0.972 with a precision of 0.004) and hygroscopicity was somewhat higher as well (1.3 with a precision of 0.01). Therefore a modest influence of sea salt, which is nonabsorbing and highly hygroscopic, can probably be seen in the larger data set.

[63] In evaluating the above measurement of ω for Asian dust, it might be questioned whether the coarse-mode aerosol is selectively lost between the nephelometer and the PSAP and/or whether the PSAP scattering response to coarse-mode dust is the same as was determined by *Bond et al.* [1999] for submicron ammonium sulfate and NaCl. To test both of these questions, we measured the PSAP scattering artifact for supermicron white powder (zinc stearate) in the laboratory subsequent to the campaign but using the same instruments and plumbing set-up (PSAP operating downstream of the nephelometer at a flow rate of 1 L min^{-1}.) The scattering correction was found to be 0.02, exactly as determined by *Bond et al.* [1999]. This indicates both that particle losses between the nephelometer and the PSAP sensing filter were insignificant at the PSAP flow rate used in ACE-Asia and that the scattering response of the PSAP is the same for irregularly shaped coarse mode aerosol as it is for spheroidal fine-mode aerosol. It is worth recalling, at this point, that the scattering correction recommended by *Bond et al.* [1999] should be made with "raw" nephelometer-measured scattering - that is, prior to correction for angular truncation. As the truncation correction for coarse-mode aerosol is around 50%, this distinction is important.

4. Conclusions and Future Work

[64] Aerosol optical properties measured from the NCAR C-130 aircraft during the ACE-Asia campaign have been presented with two general goals in mind: (1) to report new findings on the performance characteristics of nephelometer and PSAP instruments as an extension to previous ground-based studies and (2) to provide an overall characterization of the aerosol in terms of average properties, variability, and correlations among parameters. In applying these results, the issue of representativeness must not be ignored.

4.1. Instrument Performance

[65] Technical results on light scattering measurements by nephelometers and light absorption measurements by the PSAP instrument include the following.

[66] 1. Aerosol particles were sampled through a new, low turbulence inlet (LTI) that proved very effective at transmitting coarse-mode particles. LTI enhancements and plumbing losses of coarse-mode particles are estimated to largely compensate each other (Figure 4). This is consistent with independent closure studies [e.g., *Redemann et al.*,

2003], which show generally good agreement with the *in situ* coarse-mode measurements reported herein.

[67] 2. In-flight zero tests, in which the entire rack of instruments is switched to sampling particle-free air (Figures 2 and 3), facilitate the synchronization of instruments and allow noise and calibration stability to be assessed. Zero measurements at multiple altitudes permit recalibration of nephelometers in cases where significant calibration errors are discovered postflight. Replicate measurements, with dual instruments operated in parallel, provide robust measurements of noise and precision during actual measurements of aerosol scattering and absorption.

[68] 3. Nephelometer noise is normally distributed, varies with concentration (as expected), and does not vary with rate of ascent or descent (Figure 5). PSAP noise, in contrast, is not normally distributed, does not vary with concentration (again, as expected), and is sensitive to changing altitude, changing RH, and to particle loading on the internal filter (Table 2 and Figure 5).

[69] 4. A well-sealed PSAP with a clean filter used on level flight legs displays excellent noise characteristics (about 0.3 Mm^{-1} for 30-s data; Table 2b.) Techniques for sealing are given.

[70] 5. The PSAP measurement is subject to significant artifacts when sampling across large gradients in ambient RH such as transitions into or out of the boundary layer (Figure 6). These artifacts can be hand-corrected if regions of consistent optical properties can be found above and/or below the artifact region. (Eliminating this sensitivity to ambient RH by heating or drying of the sample stream might be preferable.)

[71] 6. The TSI model 3563 nephelometer displays excellent calibration stability whereas calibration drift for the Radiance Research M903 nephelometer is significant. Frequent calibrations and calibration checks (with filtered air) are therefore in order for the latter device. In addition, the Radiance Research nephelometer measured systematically lower scattering coefficients (up to 30% lower) than the TSI nephelometer for coarse-mode dominated aerosol (Figure 7).

4.2. Aerosol Characterization

[72] The nature and variability of the Asian aerosol were investigated by examining approximately 300 level-leg samples obtained over the 19 research flights. Key findings include the following.

[73] 1. When the aerosol is separated into submicron and supermicron portions, light scattering and absorption by each of these portions is seen to vary almost independently of the other (Figure 10). This confirms that the bimodal model of aerosol mass [*Whitby et al.*, 1972] is valid in this region and that a cut point of 1 μm aerodynamic diameter at low RH, as used herein, is effective at separating the aerosol into its constituent "fine" and "coarse" modes.

[74] 2. The partitioning of aerosol concentration between these two modes can be characterized by the submicron fraction of light scattering, FF_{scat} (equation (1)). Nephelometer measurements on the C-130 provide continuous information on FF_{scat} with 10-s time resolution. A very wide range of partitionings was observed (Figure 8) and this was used as the basis for a categorization scheme that captures much of the variation in intensive properties. In particular,

the wavelength dependence of scattering, å, the single scatter albedo, ω, and aerosol hygroscopicity, f_{RH}, are all strong functions of this coarse/fine partitioning (Figure 9).

[75] 3. Most variation is associated with aerosol amount, as reflected in the variation of extensive optical properties (Table 4). As shown by the ratio of measured variation to instrumental noise (Table 4), intensive properties like single scatter albedo and hygroscopicity are far less variable.

[76] 4. The intensive properties of the supermicron aerosol are very narrowly constrained while those of the submicron aerosol are somewhat more variable (Figure 11 and Table 4).

[77] 5. Two major aerosol components were encountered: fine-mode pollution and coarse-mode dust. (Rather little coarse-mode sea salt was observed, despite extensive measurements in the marine boundary layer.) Fine-mode pollution was found to be moderately absorbing (ω = 0.88 ± 0.03; mean and 95% confidence uncertainty) and moderately hygrscopic (f_{RH} = 1.7 ± 0.2), while coarse-mode dust was found to have very low absorption (ω = 0.96 ± 0.01) and to be almost nonhygroscopic (f_{RH} = 1.1 ± 0.1). Dust was observed throughout the lower troposphere, while pollution was found almost exclusively in the boundary layer (Figure 9a).

[78] 6. Two measures of the scattering phase function (the hemispheric backscatter fraction and the ratio of extinction to 180° backscatter, S) showed little sensitivity to coarse/fine partitioning (Table 4). For Fine-dominated samples, values of S were 50 ± 5 sr (mean and 95% confidence uncertainty) while for coarse-dominated samples, S was 46 ± 8.

[79] 7. Pollution appears to have significant coarse mode component in this region - cases of FF_{scat} > 0.8 were rarely observed and supermicron scattering more typically accounted for 20 to 50% of total scattering during fine-dominated events (Figure 8). As it seems unlikely that desert or agricultural dust would be so ubiquitous, the coarse mode is likely co-emitted with the pollution. Its optical properties, however, do not differ markedly from those of mineral dust.

[80] 8. Dust is usually accompanied by a fine mode that is partly the tail of the dust size distribution and partly some fairly absorbing species. Indeed, the submicron aerosol during the coarse-dominated events was more absorbing (ω = 0.82 ± 0.01; mean and 95% confidence precision) than during the fine-dominated events (ω = 0.88 ± 0.01).

4.3. Representativeness

[81] We have presented statistics on aerosol properties measured over a large region (see Figure 1) and over about six weeks of time during the spring season. To what extent do these properties represent the nature of the aerosol in the Asian outflow region rather than simply the peculiarities of this particular study? Certainly, no attempt was made at random sampling of the atmosphere; on the contrary, flight plans were deliberately designed to sample significant aerosol phenomena. Two factors, however, imposed a degree of randomness: (1) attempts to locate expected aerosol phenomena were sometimes unsuccessful and (2) various logistical constraints (e.g., flight restrictions, flying transit legs to or from a desired target, or flying in coordination with other platforms) sometimes forced the

airplane to sample along a certain track regardless of the amount of aerosol present. Despite these factors, it is likely that clean conditions (i.e., low aerosol concentrations) are systematically underrepresented in this data set.

[82]   The problem of sample bias involves many additional questions. Was spring, 2001 representative of other spring seasons? Is the spring season representative of the entire year? Did the C-130 sample the full range of air mass types and aerosol types that occur in the Asian outflow region? Did the C-130 sample each air mass and aerosol type in proportion to its true prevalence? Did the C-130 obtain a representative sampling within each air mass and aerosol type? Addressing these issues with atmospheric models, long-term data sets, and large-scale data sets (e.g., from satellites) will be important for proper application of the results herein to the larger question of climate forcing by Asian aerosols.

References

Anderson, T. L., and J. A. Ogren, Determining aerosol radiative properties using the TSI 3563 integrating nephelometer, *Aerosol Sci. Technol.*, *29*, 57–69, 1998.

Anderson, T. L., et al., Performance characteristics of a high-sensitivity, three-wavelength, total scatter/backscatter nephelometer, *J. Atmos. Oceanic Technol.*, *13*, 967–986, 1996.

Anderson, T. L., D. S. Covert, J. D. Wheeler, J. M. Harris, K. D. Perry, B. E. Trost, D. J. Jaffe, and J. A. Ogren, Aerosol backscatter fraction and single scattering albedo: Measured values and uncertainties at a coastal station in the Pacific northwest, *J. Geophys. Res.*, *104*, 26,793–26,807, 1999.

Anderson, T. L., S. J. Masonis, D. S. Covert, R. J. Charlson, and M. J. Rood, In situ measurement of the aerosol extinction-to-backscatter ratio at a polluted, continental site, *J. Geophys. Res.*, *105*, 26,907–26,915, 2000.

Anderson, T. L., R. J. Charlson, D. M. Winker, J. A. Ogren, and K. Holmén, Mesoscale variations of tropospheric aerosols, *J. Atmos. Sci.*, *60*, 119–136, 2003.

Berner, A., C. H. Lurzer, F. Pohl, O. Preining, and P. Wagner, The size distribution of the urban aerosol in Vienna, *Sci. Total Environ.*, *13*, 245–261, 1979.

Blomquist, B. W., B. J. Huebert, S. G. Howell, M. R. Litchy, C. H. Twohy, A. Schanot, D. Baumgardner, B. Lafleur, R. Seebaugh, and M. L. Laucks, An evaluation of the community aerosol inlet for the NCAR C-130 research aircraft, *J. Atmos. Oceanic Technol.*, *18*, 1387–1397, 2001.

Bond, T. C., T. L. Anderson, and D. Campbell, Calibration and intercomparison of filter-based measurements of visible light absorption by aerosols, *Aerosol Sci. Technol.*, *30*, 582–600, 1999.

Doherty, S., T. L. Anderson, and R. J. Charlson, Measurement of the lidar ratio for atmospheric aerosols using a 180°-backscatter nephelometer, *Appl. Opt.*, *38*, 1823–1832, 1999.

Gassó, S., D. A. Hegg, D. S. Covert, D. Collins, K. J. Noone, E. Öström, B. Schmid, P. B. Russell, J. M. Livingston, P. A. Durkee, and H. Johsson, Influence of humidity on the aerosol scattering coefficient and its effect on the upwelling radiance during ACE-2, *Tellus, Ser. B*, *52*, 546–567, 2000.

Gupta, R., and A. R. McFarland, Experimental study of aerosol deposition in flow splitters with turbulent flow, *Aerosol Sci. Technol.*, *34*, 216–226, 2001.

Hillamo, R. E., and E. I. Kauppinen, On the performance of the Berner low pressure impactor, *Aerosol Sci. Technol.*, *14*, 33–47, 1991.

Huebert, B. J., G. L. Lee, and W. L. Warren, Aerosol inlet passing efficiency measurement, *J. Geophys. Res.*, *95*, 16,369–16,381, 1990.

Lafleur, B. G., A low turbulence inlet for airborne aerosol sampling, M.Sc. thesis, 99 pp., Univ. of Denver, Denver, Colo., 1998.

Masonis, S. J., K. Franke, A. Ansmann, D. Müller, D. Althausen, J. A. Ogren, A. Jefferson, and P. J. Sheridan, An intercomparison of aerosol light extinction and 180° backscatter as derived using in situ instruments and Raman lidar during the INDOEX field campaign, *J. Geophys. Res.*, *107*(D19), 8014, doi:10.1029/2000JD000035, 2002.

Masonis, S. J., T. L. Anderson, and D. S. Covert, A study of the extinction-to-backscatter ratio and its relation to other aerosol optical properties during the Shoreline Environmental Aerosol Study, and comparisons to a polluted site, *J. Atmos. Oceanic Technol.*, in press, 2003.

Murayama, T., et al., An intercomparison of lidar-derived optical properties with airborne measurements near Tokyo during ACE-Asia, *J. Geophys. Res.*, *108*(D23), 8651, doi:10.1029/2002JD003259, in press, 2003.

Redemann, J., S. J. Masonis, B. Schmid, T. L. Anderson, P. Russell, J. Livingston, O. Dubovik, and A. Clarke, Clear-column closure studies of aerosols and water vapor aboard the NCAR C-130 in ACE-Asia, 2001, *J. Geophys. Res.*, *108*(D23), doi:10.1029/2003JD003442, in press, 2003.

Tang, I. N., Thermodynamic and optical properties of sea salt aerosols, *J. Geophys. Res.*, *102*, 23,269–23,275, 1997.

Weber, R. J., D. Orsini, Y. Duan, Y.-N. Lee, P. J. Klotz, and F. Brechtel, A particle-into-liquid collector for rapid measurement of aerosol bulk chemical composition, *Aerosol Sci. Technol.*, *35*, 718–727, 2001.

Whitby, K. T., R. B. Husar, and Y. H. Liu, The aerosol size distribution of Los Angeles smog, *J. Colloid Interface Sci.*, *39*, 177–204, 1972.

White, W. H., E. S. Macias, R. C. Nininger, and D. Schorran, Size-resolved measurements of light scattering by ambient particles in the southwestern U. S. A., *Atmos. Environ.*, *28*, 909–921, 1994.

―――――――――――
N. C. Ahlquist, T. L. Anderson, D. S. Covert, and S. J. Masonis, Department of Atmospheric Sciences, University of Washington, Seattle, WA 98195, USA. (tadand@atmos.washington.edu)

A. D. Clarke, S. G. Howell, and C. S. McNaughton, Department of Oceanography, University of Hawaii, Honolulu, HI 96822, USA.